Chapter 25

INFRARED ASTRONOMY

S. D. Price and T. L. Murdock

A description of the infrared celestial background is presented in this chapter with special emphasis on the 2 to 30 μm spectral region. This description is based upon comprehensive surveys of the apparently brightest sources of discrete and diffuse emission in the sky plus selective measurements on fainter objects.

25.1 OBSERVATIONAL PARAMETERS

Most astronomical observations are of the celestial position and brightness of a source at a given resolution and spectral region. These quantities may be measured as a function of time to detect variability and/or motion. Information on the spatial extent of the source depends upon the resolution of the measurement, while knowledge of the spectral energy distribution is a function of spectral resolution, and the range of wavelengths covered. Position and brightness can be determined much more accurately than distance for most objects.

25.1.1 Coordinate Systems

The position of a celestial object is measured in terms of the direction to the source projected onto a sphere of arbitrary radius—the celestial sphere. Angular coordinates are used, measured either along a great circle formed by the intersection of the sphere and a plane that includes the center, or a small circle that is formed by a plane which does not include the center.

A projection of the celestial sphere is drawn in Figure 25-1 for an observer at geographic latitude ϕ. The local vertical, defined with a plumb line, intersects the celestial sphere at the zenith z and the nadir. The horizon is the great circle perpendicular to the vertical. The celestial north and south poles are projections of the respective poles of the earth. The meridian is the visible, or upper, half of the great circle which goes through the zenith and poles and intersects the horizon at the north and south points. The celestial equator is a great circle which crosses the horizon at the east and west points.

During the course of a year, the sun appears to move along a great circle in the sky. This circle, called the ecliptic,

is a reflex of the earth's orbit projected onto the celestial sphere as shown in Figure 25-2. The ecliptic and celestial equator intersect at the equinoxes. The vernal equinox, in Figure 25-2, is the point where the sun crosses the celestial equator going south to north. The pole of the earth's rotation precesses about the ecliptic pole due to tidal forces of the sun and moon with a 26 000 yr period. This results in a westward progression of Υ of about 50 arc sec yr along the ecliptic.

Horizon (Alt-Azimuth) System: This system is unique to the observer. The azimuth, A in Figure 25-1, is the angular distance from the north point, eastward along the horizon to the vertical circle that passes through the point being considered. The altitude h is the angle from the horizon along the vertical circle. The complement of the altitude is called the zenith angle.

Celestial Coordinate System: The celestial coordinates of right ascension (α) and declination (δ) are used for stellar positions and catalogs. Since precession slowly changes the zero point of this coordinate system, the positions must be referred to a specific epoch.

The right ascension is measured eastward from the vernal equinox to the hour circle passing through the point in question. An hour circle is a great circle through the celestial poles. The declination is the angle from the celestial equator along an hour circle. Right ascension, customarily, is expressed in units of time where $1^h = 15°$ or $4^m = 1°$. Declinations are positive north of the celestial equator and negative south.

Ecliptic Coordinate System: The ecliptic plane is the plane of symmetry for objects in the solar system. The ecliptic longitude λ is measured from the vernal equinox eastward along the ecliptic. The ecliptic latitude β is the angular distance from the ecliptic along a vertical great circle. Elongation angle ε is the angle along a great circle between the sun and the point in question.

Galactic Coordinate System: The galactic plane is the geometric reference for studies of galactic structure. The galactic longitude l^{II} is the angle along the galactic plane from the galactic center. The galactic latitude b^{II} is measured along a great circle perpendicular to the galactic plane. By agreement of the International Astronomical Union, the celestial coordinates of the north galactic pole are $\alpha(1950) = 12^h49^m0$ and $\delta(1950) = + 27°24'0$, the ga-
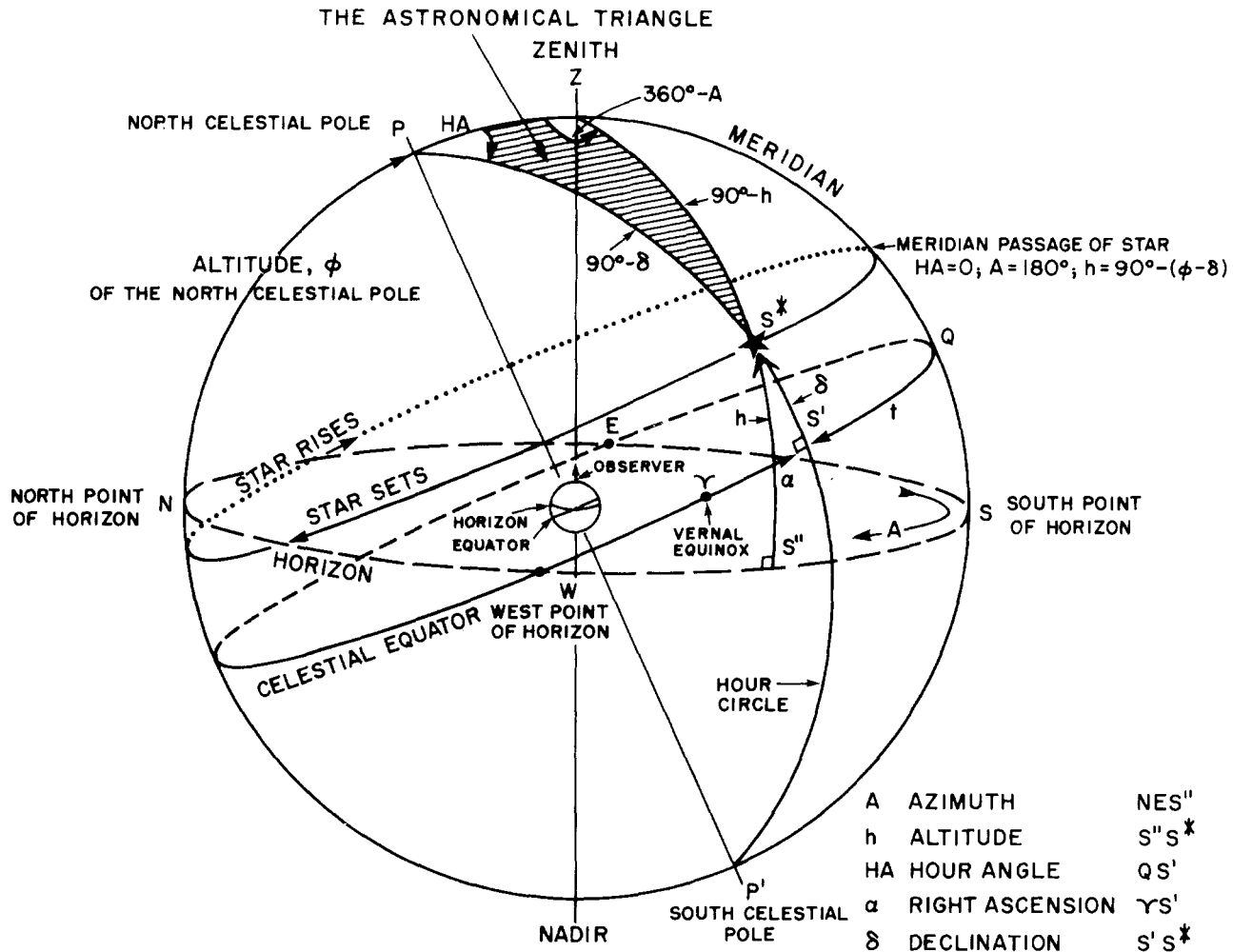
Figure 25-1. Horizon and Equatorial Coordinates. The observer is in the northern hemisphere, which places the north celestial pole at an altitude φ — the latitude of the observer. The meridian is the arc NPZS. The arc ZS* defines the vertical circle through star S* intersecting the horizon at S". The azimuth is measured along the horizon eastward from N to S". The altitude is the arc S*S" along the vertical circle through S*. The hour circle PS*P' intersects the celestial equator at S'. The hour angle is measured from the intersection of the meridian and celestial equator, Q, westward along the equator to S'. Right ascension is measured eastward along the celestial equator from Υ to S'. Declination is measured from the equator along the hour circle. The shaded triangle PZS* has the basic spherical trigonomic relations used to convert from one coordinate system to another.

lactic center at $\alpha(1950) = 17^h42^m4$ and $\delta(1950) = -28°55$ with the galactic plane inclined $62°6$ to the celestial equator.

25.1.2 Time

The time scales currently in use differ in the definition of the fundamental unit and how passage of time is measured. Ephemeris Time (ET) is a uniform measure used in gravitational theories of the solar system to calculate precise, fundamental ephermerides of the sun, moon, and planets. The fundamental unit is the tropical year defined by the mean motion of the sun in ecliptic longitude at January 0^d12^h ET 1900. Universal Time (UT) is defined by the successive

transits of celestial objects and, therefore, is related to the rotation of the earth. The fundamental unit is the mean solar day, the interval between two successive transits of the mean sun. The mean sun is defined to move at a uniform rate along the celestial equator. Sidereal time is defined by the interval between two successive transits of the mean vernal equinox. The apparent motion of the sun with respect to the stars results in the mean sidereal day being 3^m55^s9095 seconds shorter than the mean solar day. The International Atomic Time is the most precisely determined time scale in use in astronomy. It is a laboratory reference defined by the transition between two hyperfine levels in the ground state of cesium 133 at a frequency of 9 192 631 770 Hz.

The differences between Ephemeris and Universal Time are tabulated in the "Astronomical Almanac" (U.S. Gov-
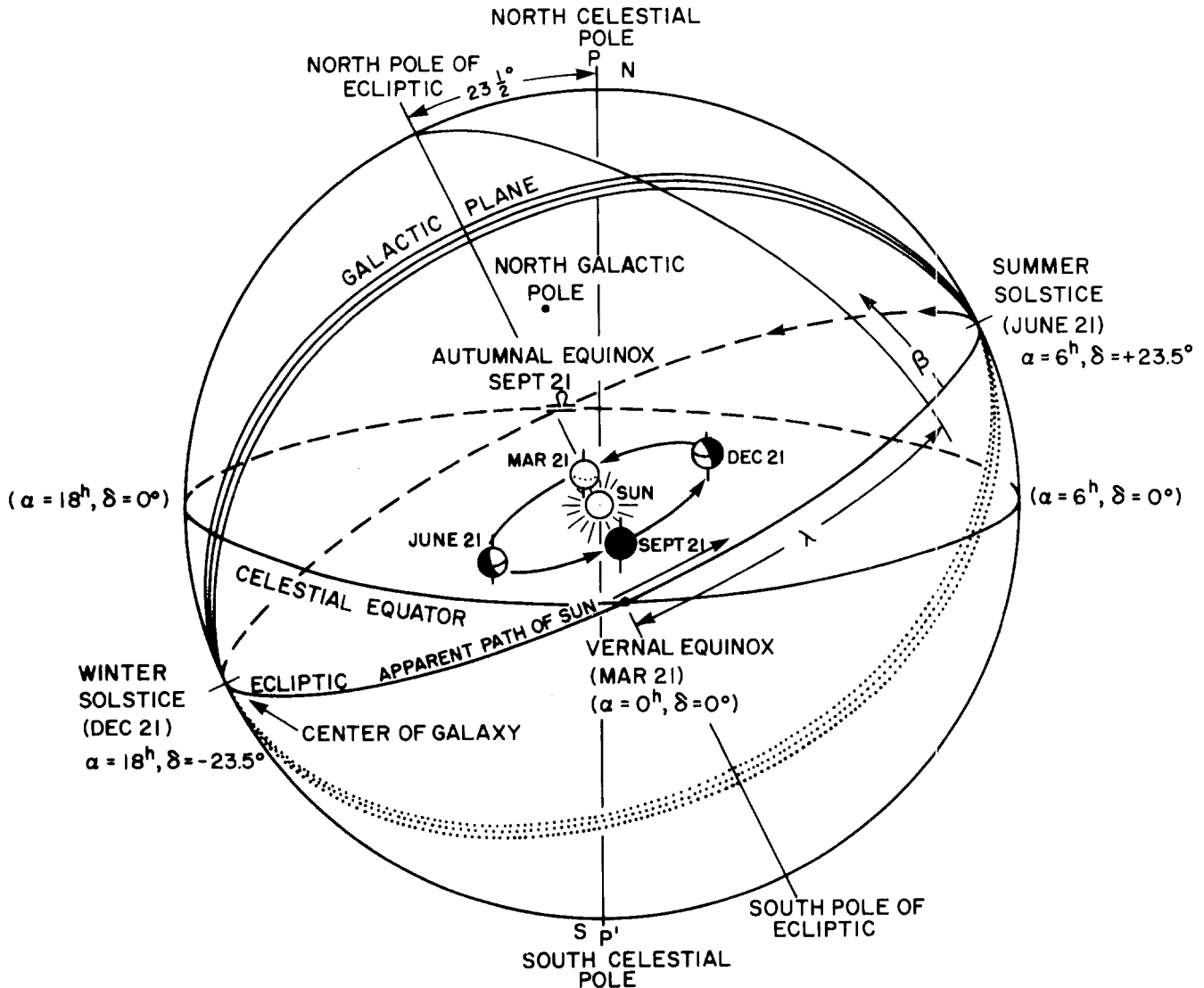
Figure 25-2. Galactic and Ecliptic Coordinate. The orbit of the earth projected onto the celestial sphere defines the ecliptic plane. The ecliptic pole is inclined 23°44 from the celestial pole. By definition, the intersection of the ecliptic and equatorial planes is the zero point for right ascension and ecliptic longitude, λ. The north galactic pole is some 63° from the celestial pole.

ernment Printing Office) as is the difference between International Atomic Time and Coordinated Universal Time (UTC). UTC is the scale available from broadcast signals.

25.1.3 Intensities—Magnitude

Absolute intensity measurements by direct comparison with laboratory standards exist for only a few astronomical objects. Instead, intensity measurements are referred to one or more secondary standard stars. The secondary standard stars are a network of non-variable stars roughly uniform in distribution across the sky which have accurate photometry with respect to each other. These secondary standards are referenced to a small number of primary standards, stars which have absolute flux determinations from laboratory calibrated sources.

Johnson [1965] used the sun as a standard with the obvious problem of transferring the very bright extended source to fainter intensity. Vega, α Lyr, is currently the most common star chosen for a primary standard. Absolute calibration of α Lyr through direct comparison with laboratory standard sources covers the wavelength from 0.35 to 1.08 μm to an accuracy of better than 3% [Hayes and Latham, 1975; Tug, White, and Lockwood, 1977]. Low [1973] has obtained the absolute 11 μm flux on 3 stars to 10% accuracy by comparison with laboratory standards.

Stellar intensities are often expressed in terms of mag-

nitude, a logarithmic scale referenced to an adopted standard. The apparent brightness ratio, I_2/I_1, of two stars of apparent magnitudes m_2 and m_1 is

$$I_2/I_1 = 10^{-0.4(m_2 - m_1)}$$

and (25.1)

$$m_2 - m_1 = -2.5 \log (I_2/I_1).$$

The absolute magnitude M is defined as the apparent magnitude a star would have at a distance of 10 parsecs ($3.085678 \times 10^{+19}$ cm). The absolute and apparent magnitudes are related by

$$M = m + 5 - 5 \log r - A \qquad (25.2)$$

with r = the stellar distance in parsecs and A the interstellar extinction, in magnitudes, to the star.

The measured magnitude also depends on the spectral energy distribution of the star through the spectral sensitivity of the detector. The spectral selectivity of the measurement is usually expressed by the system unique parameters of effective wavelength λ_c and effective bandwidths $\Delta\lambda_c$ defined by

$$\lambda_c = \frac{\int_0^\infty \lambda \, S_\lambda \, d\lambda}{\int_0^\infty S_\lambda \, d\lambda},$$

and (25.3)

$$\Delta\lambda_c = \int_0^\infty S_\lambda \, d\lambda$$

with S_λ the system spectral response.

The effective wavelengths, effective bandwidths, and flux for a zero magnitude star within the respective band passes are given in Table 25-1 for a widely used system of photoelectric photometry. The photometric bands in the infrared coincide with atmospheric transmission windows.

25.1.4 Distance

Direct radar returns and radio transmission from interplanetary space probes lead to very accurate distance determination within the solar system. Distances to nearby stars can be calculated from trigonometric parallax, the stellar displacement as viewed from different locations of the earth's orbit around the sun. More distant stars require indirect methods for calculating distance, which depend on the statistical properties of a group of stars and the apparent brightnesses of "standard candles".

Table 25-1. Definition of zero magnitude flux as function of wavelength. [Johnson, 1965; Low, 1973]

Band	λ_c (μm)	$\Delta\lambda_c$ (μm)	Flux (m(λ_c) = 0) W cm$^{-2}\mu$m^{-1}
U	0.365	0.068	4.27×10^{-12}
B	0.44	0.098	6.61×10^{-12}
V	0.55	0.089	3.72×10^{-12}
R	0.70	0.72	1.74×10^{-12}
I	0.88	0.24	8.32×10^{-13}
J	1.25	0.38	3.31×10^{-13}
H	1.65	0.30	1.28×10^{-13}
K	2.22	0.48	4.14×10^{-14}
L	3.6	0.70	6.38×10^{-15}
M	5.0	1.73	1.82×10^{-15}
N	10.6	4.33	8.7×10^{-17}
Q	21	5.8	6.5×10^{-18}

25.1.4.1 Parallax. The trigonometric parallax is defined as the angle, p or π, subtended by the mean radius of the orbit of the earth at the distance of the star. As of 1980 some 11 600 stars have parallaxes measured with varying degrees of accuracy; only 10 stars have parallaxes determined to better than 2% [Upgren, 1980].

A parsec pc is the distance at which the parallax is one arc second. It is numerically the inverse of the parallax and, as such, is an independent measure which scales by the value of an astronomical unit (equals mean distance between the earth and sun). By definition 1 pc = 206264.802 AU From Allen [1973] 1 AU = 1.495979×10^{13} cm; thus 1 pc = 3.085679×10^{18} cm.

Beyond 50 to 100 pc where trigonometric parallaxes are unreliable, distances can be inferred from the observed motion of stars. The measured quantities are the proper motion, the observed angular motion pependicular to the line of sight, and the radial velocity, which is determined from the Doppler shift of the spectral lines. The tangential velocity can be determined from the proper motion and radial velocity if the direction of the total velocity vector is known. Various methods based on statistical arguments for an aggregate of stars are used to estimate the direction of the total velocity vector or the value of v_t directly. These procedures are valid out to 100 to 200 pcs but may be extended to a kiloparsec using a reasonable theory of galactic rotation.

25.1.4.2 Standard Candles. The distance modulus (M-m) can be derived from the observed apparent magnitude and knowledge of the absolute magnitude or intrinsic brightness of a source. An estimate of the interstellar extinction will then produce a distance through Equation (25.2).

Spectroscopic Parallax: The intensity ratios of certain luminosity sensitive spectral lines correlate well with the absolute magnitude of those stars which have accurately determined parallax. For those stars bright enough for a

high dispersion spectrum to be obtained, the spectroscopic parallax is derived from the spectroscopic estimate of the absolute magnitude and the observed apparent magnitude.

Variable Stars: Stars that vary in brightness in a distinctive manner can be seen to large distances and are useful distance indicators when their absolute magnitude can be related to the variability.

The absolute magnitudes of novae at maxima are correlated with the time rates of decay in the light curves. Furthermore, the absolute brightness of the light curves are calibrated from the novae close enough to have expansion parallaxes, that is, the angular expansion rates and radial velocities of the ejected material are measured and a distance derived assuming spherical symmetry.

As a class, the cepheid variables exhibit an empirical relationship between absolute magnitude and period of pulsation. The various cepheid subclasses—classical and dwarf cepheids, RR Lyrae, δ Sct, W Vir, β CMa and β Cep stars—differ in the shape of the light curve, amplitude, and temperature variation during pulsation. The absolute magnitudes for these stars are derived from statistical parallaxes and stellar evolution models applied to the clusters which contain them.

25.1.4.3 Dynamic Distances.

A theory of galactic rotation may be used with radial velocity measurements to obtain distances greater than a kiloparsec. This technique has been extensively exploited in radio astronomy particularly for HII regions and molecular clouds.

In the simplest case, galactic constituents are assumed to move in circular orbits with a decreasing angular velocity with increasing distance from the center. At a given longitude in the galactic plane, the largest observed radial velocity is at the point where the line of sight is closest to the galactic center. A rotation curve, in terms of the galactocentric distance of the sun, $\bar{\omega}_0$ is constructed from the maximum observed radial velocity as a function of longitude. This curve can be used to derive distances relative to $\bar{\omega}_0$ from the observed radial velocities. If the measured radial velocity is smaller than the maximum, the positional ambiguity is resolved by assuming that the larger, brighter objects are closer.

25.1.4.4 Extragalactic Distances.

Primary indicators of extragalactic distances such as novae and cepheid variables are calibrated by fundamental means within our own galaxy. These so called primary standards are good out to about a Megaparsec (Mpc). Overlapping, and calibrated by the primary indicators, are less reliable indicators such as the brightest stars in a galaxy and the size and brightness of HII regions. These are observable out to about 10 Mpc. At distances greater than 10 Mpc isophotal galactic diameters and galactic luminosity class are used for distance determination.

At very large distances the radial velocity is, on the average, directly proportional to the distance. The constant of proportionality, the Hubble constant H reflect the expansion rate of the universe. If the Hubble constant is known then a measure of the radial velocity of a galaxy results in a distance. Various recent determinations of the Hubble constant range from 50 to 100 km s^{-1} Mpc^{-1}.

25.2 THE SOLAR SYSTEM

Our knowledge and understanding of objects in the solar system have advanced spectacularly over the past decade with the fruition of the space exploration programs and the development of new measurement techniques. This section presents a description of the solar system as seen at wavelengths between visual and 30 μm from a point near the earth but above the atmosphere.

Objects in the solar system scatter and absorb sunlight. In the visible, this scattered sunlight has a spectral distribution similar to that of the sun, a 6000 K blackbody with absorption and emission lines, but modified by the spectral reflectivity of the body's surface. The object is warmed by absorbed sunlight and consequently emits thermal radiation. This thermal re-emission is characterized by the Planck equation appropriate to the temperature and modified by the spectral emissivity of its surface layers. Thermal emission arises from the topmost layers, which are opaque or semi-opaque at the wavelength in question. In the simple case of a body with no atmosphere, the thermal emission spectrum is determined by the temperature, the physical structure, and the chemical composition of the emitting layer. The asteroids, most planetary satellites, Mercury and the moon fall into this category. If the atmosphere of the body is optically thin, the infrared thermal emission is not appreciably altered and measurements of the spectral intensity continues to provide information about the surface layers. At the other extreme, if the atmosphere is completely opaque, infrared emission reveals the character and state of the atmospheric layers which are optically thick at the measured wavelength. Venus, Jupiter, Saturn, Uranus and Neptune are clear examples of objects in this category. The atmospheres of objects intermediate to these extremes are optically thick only at some wavelengths, and the spectral emission is a superposition of reflected sunlight and thermal emission from the surface and atmospheric emission and absorption. Mars and comets are examples of this class. Finally, an optically thin dust cloud is present in the solar system. The zodiacal light is scattered sunlight and thermal emission from the dust grains in this cloud.

25.2.1 Objects with Negligible Atmospheres

To first approximation, a typical object in the solar system does not rotate and is located at a constant distance, R, from the sun. Assume that there are no internal sources

of heat, that the surface cannot conduct heat away, and that the surface is in equilibrium with sunlight. At the subsolar point of such an object, the equilibrium surface temperature is given by the heat balance between absorbed sunlight and radiated thermal emission

$$T_0 = \frac{(1 - A)}{\varepsilon_{IR}\sigma} \left(\frac{E}{R^2}\right)^{1/4} \qquad (25.4)$$

where

A = Bond Albedo (ratio of total incident to reflected light for a spherical body)

E = Solar constant at 1.0 AU = .1368 W/m^2

ε_{IR} = Infrared average emissivitiy

σ = Stefan-Boltzmann Constant = 5.66956 $\times$ 10^{-12} Wcm^{-2}deg^{-4}.

The temperature distribution on a non-rotating spherical surface will be isothermal concentric bands around the subsolar point. If the subsolar point is defined to be the thermal pole, the temperature at thermal colatitude ϕ is

$$T(\phi) = T_o \cos^{1/4} \phi. \qquad (25.5)$$

For an object with a rotation period P an isotropic surface material with uniform density ρ, specific heat c and thermal conductivity K, the temperature distribution inside the object is determined by the heat conduction equation

$$\rho c \frac{\partial T}{\partial t} = K \nabla^2 T. \qquad (25.6)$$

The boundary condition on the surface in sunlight is

$$\varepsilon_{IR} \sigma T_s^4 - \frac{(1 - A)}{R^2} E \cos \phi = K\nabla T_s, \qquad (25.7)$$

while on the dark side

$$\varepsilon_{IR} \sigma T_s^4 = K\nabla T_s. \qquad (25.8)$$

If the rotational axis lies in a plane perpendicular to the incident sunlight, the thermal pole traverses the rotational equator, and thermal emission from the dark side arises from thin isothermal longitudinal stripes whose temperature falls to a minimum just before local dawn. The minimum temperature is determined by the rotational period and by the thermal properties of the uppermost several meters of the surface material. Typical minimum temperatures for the moon and Mercury are about 100 K, indicating a loosely packed, dusty, dielectric surface material.

For the more realistic case of an atmosphereless object

with a solid bedrock overlain by varying depths of dust and broken rock, K, ρ, and c are not constant. The conduction equation must also be modified to include radiation between the dust grains, which is a major heat transport mechanism in this case. Furthermore, rocks which protrude through the dusty surface have been shown to introduce significant discrepancies between the predictions based on the simplified models discussed above and infrared measurements of the lunar terrain during eclipse [Allen and Ney, 1969] and the planet Mercury near inferior conjunction [Murdock, 1974].

If the field of view of a measurement is larger than the apparent solid angle subtended by the body, the resulting spectrum is the superposition of scattered sunlight and thermal emission from the visible surface, each region weighted by the respective apparent projected area. The phase angle i is the angle between the sun and the observer as seen from the center of the object. The fraction of the illuminated side seen by the observer is

$$k = 0.5 (1 + \cos i).$$

Objects with orbital radii less than that of the observer will go through all phases $0 \leqslant k \leqslant 1$. Objects with orbital radii larger than the observer will go through partial phases $k_{min} \leqslant k \leqslant 1$. The phase angle may be calculated from

$$\cos i = \frac{R_{eo}^2 + R^2 - R_e^2}{2 R_{eo} R}, \qquad (25.9)$$

where

R_{eo} = true geocentric distance in AU

R_e = true Earth-Sun distance in AU

R = heliocentric distance of the object in AU.

Values of phase angle and the orbital distances for various solar system objects are tabulated in the "Astronomical Almanac."

Color temperature T_c is defined as the temperature of the Planck function B(λ,T) that best fits the measured spectral shape. Brightness temperature T_b at any wavelength λ is defined as that temperature which satisfies

$$I(\lambda) = B(\lambda,T_b) \Omega_c,$$

where I(λ) is the measured spectral intensity and Ω_c is the emitting solid angle. For simple objects in solar orbit, the emitting solid angle required to bring the color and brightness temperatures in the midinfrared into agreement is, to good approximation

$$\Omega_c = k\Omega,$$

where Ω is the total solid angle subtended by the body and k is the fraction of the sunlit surface visible from earth.

Thus, the sunlit portion of the disk dominates the total thermal emission at these wavelengths.

The effective brightness temperature at wavelength λ_c is found from

$$I(\lambda_c) = B(\lambda_c, T_c) \, \Omega_c.$$

The effective brightness temperature can be normalized to the mean sun-object distance R_s, by

$$T_s(\lambda) = T_c(\lambda) \left(\frac{R}{R_s}\right)^{1/2}.$$

The apparent brightness of the object varies with distance from the earth through the relation

$$I(\lambda) = I(R_{eo}, \lambda) \left(\frac{R_{eo}}{d}\right)^2,$$

where R_{eo} = true geocentric distance at the time of measurement and d = desired geocentric distance.

25.2.1.1 Mercury. Mercury's orbit is highly eccentric and its infrared spectrum varies not only with phase angle but also with solar distance. The subsolar point temperature variation from aphelion to perihelion is from 575 to 710 K. At phase angles less than 160° the effective emitting area required to bring the brightness temperature into agreement with the color temperature is the solid angle of the visible sunlit portion of the apparent disk. At phase angles greater than 160°, the contributions from hot rocks in the partially lit crescent and the dark side become significant. The warm color temperature of the crescent is due to crater walls and raised rocks on the surface, which remain in sunlight longer than predicted by the $\cos^{1/4}\theta$ variation for a smooth spherical surface. These objects cool at a slower rate than the rest of the surface material. Approximately 3% of the crescent solid angle is required to make the crescent color and brightness temperatures equal. The minimum effective temperature of 106 K observed for the dark side [Murdock and Ney, 1970] is indicative of a dusty, loosely packed surface. Phase curves of the visual, λ = 3.6, 10.8, and 20 μm emission for Mercury at mean solar distance (R = 0.387AU) corrected to a constant geocentric distance of 1.0 AU [Murdock, 1974] is given in Table 25-2.

25.2.1.2 The Moon. The lunar surface is primarily composed of a loosely packed dielectric dust quite similar in thermal and visual properties to the surface of Mercury. Pictures of the moon and Mercury are remarkably similar as are their visual and infrared phase curves [Ryadov, Furashov, and Sharonov, 1964; Pikkarainen 1969; Murdock 1974]. The lunar albedo is 0.07 [Allen, 1973] and the subsolar point temperature varies between 397 K and 391 K from perihelion to aphelion. Allen [1970] found that ap-

Table 25-2. Mercury magnitudes at 0.387 AU from the sun, 1.0 AU from the earth.

θ	0.54μm	3.6μm	10.8μm	20μm
0	-2.5	-9.0	-13.0	-12.9
20	-1.8	-8.8	-12.7	-12.7
40	-1.2	-8.3	-12.3	-12.5
60	-0.7	-8.0	-11.9	-12.3
80	-0.1	-7.4	-11.2	-12.1
100	$+0.6$	-6.2	-10.6	-11.9
120	$+1.6$	-4.9	-9.3	-11.4
140	$+3.0$	-3.1	-8.0	-11.0
160	$+4.9$	$+0.3$	-5.8	-10.4

proximately 3% of the average lunar surface and as much as 10% of crater areas must be exposed rock in order to account for the lunar thermal anomolies found by Shorthill and Saari [1965]. Thus the infrared appearance of the Moon would be nearly identical to that of the planet Mercury at the same solar distance and the shapes of the phase curves for the two objects can be assumed to be similar. The lunar full disk λ_c = 11.4 μm brightness at i = 0° is M = -22.5.

25.2.1.3 Asteroids and Planetary Moons. As of January 1984, 2992 asteroids are listed with orbital elements in the "Minor Planets Circulars" published on behalf of Commission 20 of the International Union. In general, the asteroids have albedos between 0.065 and 0.23 [Gradie and Tedesco, 1982]. The infrared spectral energy distributions between 5 and 30 μm for asteroids are quite similar to those of gray bodies [Gillett and Merrill, 1975; Hansen, 1977]. A decrease in emissivity from 20 to 85 μm has been observed for some asteroids [LeVan and Price, 1984]. The asteroid distribution is concentrated to the ecliptic plane with an exponential folding height of about 7°.

The planetary moons are an inhomogeneous set of objects. The Mariner, Pioneer, Voyager, and Viking series of exploration experiments have shown that each object has a unique spectral signature. Typical Bond albedos range between 0.2 and 0.7 for ice covered or dust covered satellite surfaces [Hansen, 1977, Smith et al., 1981].

25.2.2 Objects with Optically Thick Atmospheres

Emission from objects with optically thick atmospheres comes from those depths which are opaque at the wavelength in question. The visual and infrared spectra of these objects are complex superpositions of scattered sunlight and molecular vibration and rotation band emission over an underlying continuum which can be approximated by a gray body spectrum. In general, thermal radiation at different infrared wavelengths comes from different atmospheric depths and results in different effective brightness temperatures.

Table 25-3. Planets with optically thick atmospheres, compiled from data given in Stier et al. [1977], Wright [1976], Reed et al. [1978], Ward et al. [1977], Erickson et al. [1978], Tokunga et al. [1977], Gillett and Forest [1974], Hanel et al. [1981], Allen and Murdock [1970] and Courten et al. [1978].

	A	T_{eq}	T_{eff}	T_{10}	T_{20}	T_{30-250}
Venus	0.77 ± 0.07	228 ± 5	240 ± 5		200–250	245
Jupiter	0.35 ± 0.07	111	125 ± 3	124	125	130
Saturn	0.50 ± 0.03	76 ± 1	94.4 ± 3	110	92	85.6 ± 3
Titan	0.21	86	110	126	110	
Uranus	0.31 ± 0.35	58.5	58.5	133 ± 4 at 5μm	54.7 ± 1.8	58.5
Neptune	0.33	46	59.7	115 at 7.5μm	60	59.7 ± 4

A = Bond Albedo
T_{eq} = Equilibrium Temperature
T_{eff} = Effective Temperature
T_{10} = 10 μm Brightness Temperature
T_{20} = 20 μm Brightness Temperature
T_{30-250} = Brightness Temperature in the 30–250 μm Region

The visual appearance of these objects varies from the smooth featureless cloud tops of Venus to the brightly banded turbulent clouds of Jupiter. Table 25-3 summarized the visual and infrared properties averaged over the disk for this class of object.

25.2.3 Objects with Semi-Transparent Atmospheres

The third class of objects in the solar system consists of those bodies with semi-transparent atmospheres. The surface emission is modified or blocked at some wavelengths, and the observed spectral intensity originates in both surface layers and the atmosphere.

25.2.3.1 Mars. The Martian atmosphere is optically thin. At wavelengths between 30 and 300 μm the mean transmission is between 85% and 95%. The atmospheric effects are also small at the shorter infrared wavelengths. The predominant result is that the product $(K \rho c)^{1/2}$ of the Martian surface is three times larger than that for Mercury and the Moon. The Martian albedo averaged over the disk is 0.10 and the $\lambda_c = 10$ μm effective brightness temperature varies between 230 K and 270 K with phase angle and solar distance variations [Wright, 1976].

25.2.3.2 Comets. Comets appear to originate in deep space beyond the orbit of Pluto. Chance gravitational encounters with nearby stars or each other propel several of these objects per year into the outer solar system. Gravitational interactions with the giant planets send the comets into the inner solar system on parabolic or hyperbolic orbits. Encounters with the planets can also modify these open orbits into closed long period ellipses. Since the comets originally condensed from the solar nebulae at such large distances
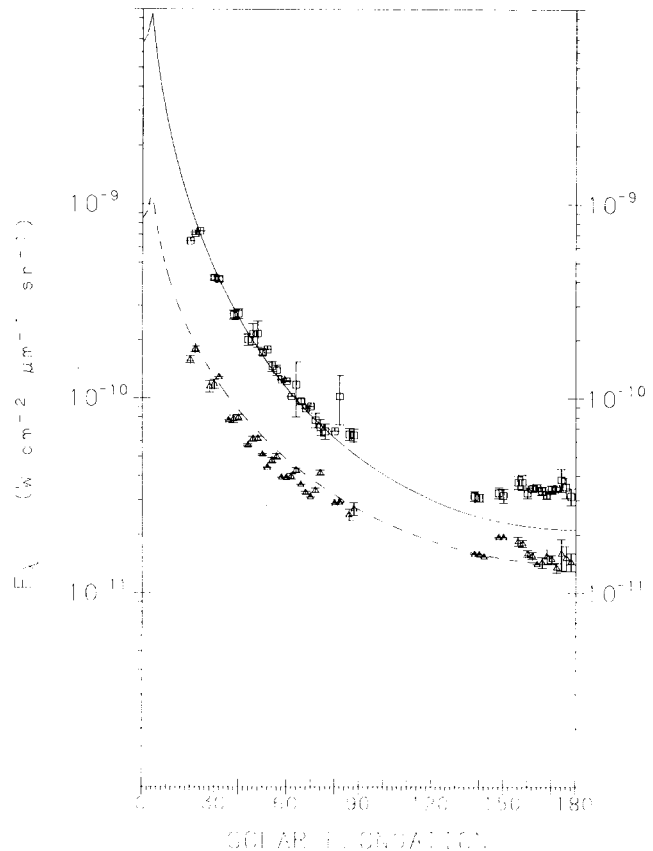

Figure 25-3. Variation of the zodiacal emission at 10.9 μm (squares) and 20.9 μm (triangles) along the ecliptic plane. Solid and dashed lines are the model predictions at the respective wavelengths from Equation (25.10).

from the sun, they appear to have lost very few of their volatile compounds and seem to be light, porous clumps of frozen gases and dust grains. New comets which have never approached the sun should have retained most of their original accretion structure. As the comet moves closer to the sun it begins to warm, sheds its outer layers and probably changes its internal structure by melting. The dust and gas that has been removed from the outer layers escapes from the core and follows its own solar orbit trajectory as the comet tail and anti-tail. Typical radii of the comet nucleus range between 5 and 30 km with albedos about 0.18 [Ney, 1974].

25.2.4 The Zodiacal Light

A low density cloud of dust surrounds the sun. This cloud is concentrated toward the eliptic plane of the solar system and extends inward from the orbit of Jupiter to a

minimum solar distance determined by the sublimation temperature of the dust grains. Sunlight scattered from these grains appears as a diffuse background glow in the night sky. This glow is brightest toward the sun and is centered near the ecliptic plane. The zodiacal light has been observed visually since ancient times and systematically studied since the late 1600s. Satellite observations and ground based studies of the visual zodiacal light have been used in conjunction with data from the Pioneer and Helios space probes to define the extent and apparent angular distribution of the dust cloud [Leinert, 1975]. Recently, infrared measurements taken during rocket flights and satellite experiments have returned the first definitive infrared observations of the clouds thermal emission spectrum [Soifer et al., 1971; Price et al., 1980; Murdock and Price, 1984; Hauser et al., 1984].

The observed variation in the 10.9 and 20.9 μm radiance along the ecliptic plane is shown in Figure 25-3. The plane to pole changes in these radiances are shown in Figure 25-4 for a sun centered longitude of 45°. Infrared spectrophotometry of the zodiacal emission at a sun centered longitude of 60° and at the north ecliptic pole in the summer is shown in Figure 25-5.

The dynamics of small particles in the solar system are [Leinhert, 1975] as follows. The solar gravitational acceleration is opposed by the centripetal acceleration from the orbital velocity and outward radiation pressure of incident sunlight. The radiation pressure exceeds the gravitational
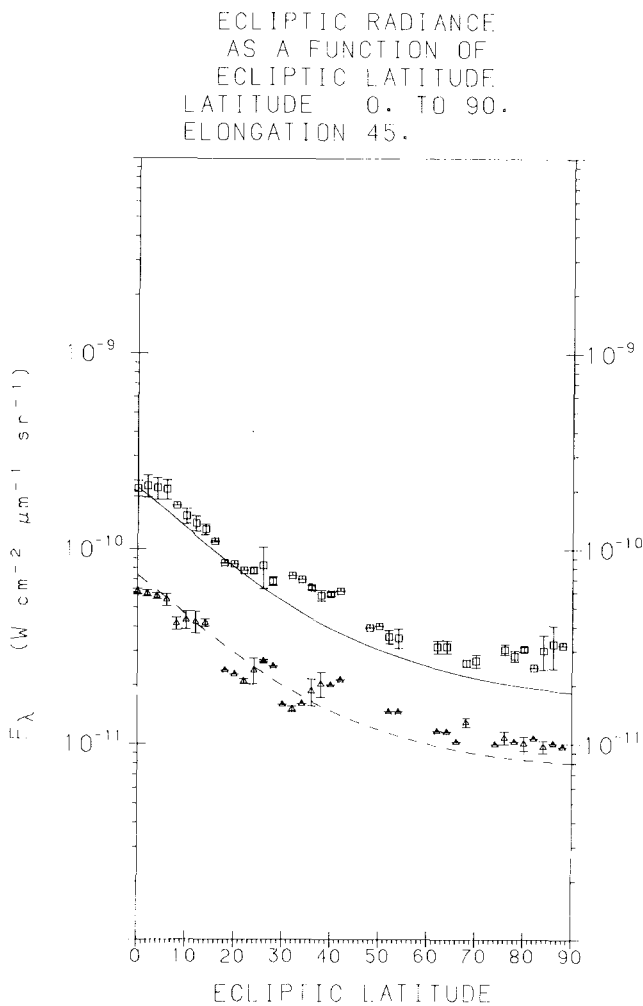

Figure 25-4. Plane to pole variation in the 10.9 and 20.9 zodiacal radiance at an elongation of 45°. Symbols are the same as in Figure 25-3.
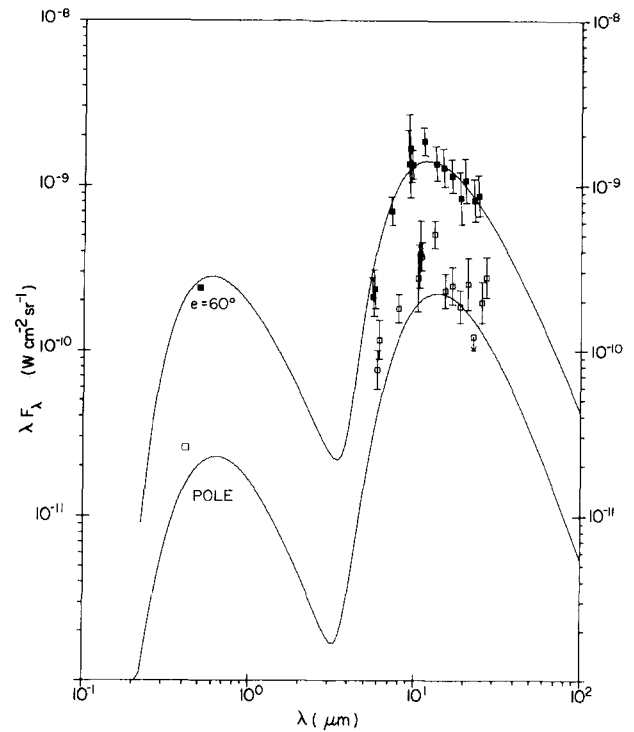

Figure 25-5. Spectrophotometry of the zodiacal light at the ecliptic pole and in the plane at 60° elongation. Visual values are from Allen [1973].

force for particles smaller than 0.2 μm in diameter and these particles are blown out of the solar system. A braking force (Poynting-Robertson effect) due to the small aberration of sunlight decelerates a small particle in the solar system causing it to slowly spiral into the sun. As the dust particle nears the sun it warms up, subliming until it is small enough to be driven out of the solar system by radiation pressure. A typical dust grain has a radius of 1.0 μm and takes about 10^4 years to be ejected from the solar system after injection.

The spectral energy distribution of the zodiacal light is a superposition of scattered sunlight and thermal emission from all the particles along the line of sight. The scattered sunlight at a solar elongation of 90° in the ecliptic plane can be represented by the solar energy distribution diluted by 9×10^{-14} [Allen, 1973]. The infrared energy, $j(\lambda)$, in a solid angle, dω, from the dust in the solar system is the sum of the thermal emission and scattered sunlight and is given by

$$j(\lambda) = \int_0^x dl \int_0^x ds\ N(D,Z,s)\ \pi\ s^2 \left[Q_{em}\ (\lambda,s)B(\lambda,T_p) \right.$$

$$\left. + Q_{sc}(\Theta, \lambda,s)F\ (\lambda) \left(\frac{R_s}{D} \right)^2 \right]\ d\omega$$

$$(25.10)$$

dl = increment along the line of sight

Q_{em} = emission efficiency = $\epsilon(\lambda)$ emissivity

s = particle radius

T_p = particle temperature

N = number density at an in plane distance of D from the sun and z above or below the plane

$F(\lambda)$ = infrared solar energy distribution

D = projection of solar distance, R, of particle into the ecliptic plane

Z = height of particle above the plane

$R^2 = D^2 + Z^2$

$Q\ (\lambda_{sc},S,\Theta)$ = scattering efficiency = $\dfrac{a(\lambda)}{4\ \pi}$ P(Θ) with

$a(\lambda)$ = albedo of the particle.

The integral in Equation (25.10) is heavily weighted for near earth conditions and a mean value of emissivity ($\epsilon = 0.7$), albedo ($a = 0.3$) and particle area times density ($s^2N_o = 6.44 \times 10^{-22}$cm^{-1}) reasonably represent the observed data. Separating the spatial density variation into an exponential vertical distribution and a power law in plane distribution Equation (25.10) fits the observed data if

$$j(\lambda) = 1.4 \times 10^{-21}\text{cm}^{-1} \int_0^x dl \left[\frac{D}{R^2} \exp \left\{ -2.6\frac{|z|}{R} \right\} B(\lambda,T_p) \right.$$

$$\left. + 0.137P(\Theta)F(\lambda) \left(\frac{R_c}{R} \right)^2 \right] d\omega \qquad (12.11)$$

where P(Θ) is the scattering coefficient in terms of Legendre polynomials P(Θ$_o$) = P$_0$(cosΘ) + 1.3054 P$_1$(cos Θ) + 1.3014 P$_2$(cos Θ).

This expression was used to calculate the model fits in Figures 25-3 through 25-5. Table 25-4 lists the observed 10.9 and 20.9 radiances as a function of ecliptic elongation and latitude in 5° bins in each coordinate. Satellite measurements [Hauser et al., 1984] are 40% higher at the ecliptic pole and a factor of two higher in the plane.

Satellite observations [Low et al, 1984] indicate the presence of three roughly parallel bands of excess zodiacal emission located at − 10°6, − 2°8 and 9° latitude. The 160– 200 K color temperature of this excess emission is characteristic of the main asteroid belt. This argues for an asteroidal origin for the zodiacal dust. The infrared spectra of the zodiacal emission is consistent with dust found in comet tails. The origin of the interplanetary dust is still not resolved.

25.3 THE GALAXY

The galaxy is composed of stars and clouds of gas and dust in roughly equal proportion by mass. It is lenticular in shape with an ellipsoidal bulge and a surrounding disk with an almost exponential decrease in brightness and mass with distance from the center. The gas has an exponential scale height of about 4 kpc, the stars 2-3 kpc. There is evidence for a spiral pattern in the disk. A sparse scattering of single stars and clusters of stars (globular clusters) are spherically distributed about the galactic center in the galactic halo. The sun is about 8.5 kpc from the galactic center and travels at a speed of about 225 km/s.

25.3.1 Stars

Stars may be grouped into four general categories according to size, luminosity, and density. Most stars are dwarf or main sequence stars. Within 20 parsecs of the sun 90% of all stars, including the sun, are dwarfs. White dwarfs are stars of low luminosity, high temperature, and very high density. They constitute about 8% of the nearby stars. Giant stars are large objects of low density and high intrinsic luminosity. Although they account for only 0.7% of the stars in the solar neighborhood, they dominate the bright end of the source counts because of their high luminosity. Supergiant stars are extremely bright stars of very low density, up to 100 times more luminous and 10 times larger

Table 25-4a. Zodiacal Radiance at 10.9 μm. Units are 10^{-12} $Wcm^{-2}\mu m^{-1}sr^{-1}$.

LATITUDE	0°				25°							50°				75°						
90																						
85	35	32	33	34								25	28	26		25		25				
80	27	29			37	37				27	26								28	28	27	28
75	32	33	30	29	34	28						30				29	29	28	28	28	30	29
70	29	30	31		31	32	32	43				31	31	31		29	28	28	27	31	35	30
65	38	36	33	31	30	32	30	45				32	31	31		33	30	30	32		30	29
60		36	34		31	38	34	48	50			33	31			32	34	30	31	30	32	33
55	38			37	42	34	42	38	52	35		34	31			33	34	32	36	35	35	33
50	39	34			40	36	50	40	55	36		37	35			35		35	34	34	38	36
45			42		43	46	52	49	54	49	48	43	36			37	37	35	46	42	43	40
40				60	47	50	51	67	50	60	46	41	41			39	49	43	46	43	40	40
35			55				65	57	65			50	47	41		53	50	46	49	43	40	39
30				72	75	66	65	79	65	72	60	49	58			66	56	50	47	43	45	40
25				90	69	81	91	79	77			83	65	57		84	72	49	51	48	43	60
20	150	115			140	106	95	101	87			92	71	86		74	63	56	54	51	54	42
15	189				167	144	146	132	114			107	93	88		73	74	64	57	61	44	46
10					339	244	226	184	160			158	126	122	92	82	73	69	63	49	57	59
5	507				428	367	250	220				194	165	132	104	89	74	73	68	70	62	65
0					700	415	260	269	216			190	143	117		106	82	72	68	68	64	

Table 25-4a (continued).

LATITUDE	100°				125°					150°								
90																		
85	27				26					22	26		25	25	24			
80	28	27	28	36	27	28	27	27		29	28	29	29			24	23	
75	29	28	29		30	27	27	28	28	27	26	27		29	28	31	24	
70	30	28	28	29	28	28	28	27	26			28	27	29	30	29	28	
65	30	29	31	29	34	29				27			27	29	31			
60	34	33	30	29	29	31	31	31	30					30	29		34	
55	32	33	31	33	33	34	35	32	29	29			32					
50	40	36	36	34	31	30	30	30	29	28	30	31	35	30				
45	38	37	37	37	35	35	31	30	28	32	27	30	28	29	31			
40	35	36	35	34	31	31	37	34	33	29	29	29	27	29	29	35		
35	34	35	33	32	32	32	31	31	33	34	30	29	27	29	29	30	28	
30	40	47	38	37	36	35		32	32	31	31	35	27	29	29	29	28	
25	52	38	36	35	38	38	36	36	36	33	28	36	31	30	29	28	30	
20	45	42	42	37	34	34	34	35	35	36	30	33	31	32	29	31	33	
15	40	34	33	33	34			34	33		35	31	31	34	35	25	32	33
10	59						34	32		33	33	35	31	33	34	35	32	32
5								33	33	32	31	31	33	33	34	34	36	35
0							34	31	36	32	35	34	33	34	38			

Table 25-4b. Zodiacal Radiance at 20.9μm. Units are $10^{-12}\,\mathrm{Wcm^{-2}\mu m^{-1}sr^{-1}}$.

LAT.	0°	25°	50°	75°
90				
85	12 10 11		11 10 10 10 11	11
80	11 10	10 9 10 10 10		10 11 11 10 11
75	10 10 10 9	10 10	12 11 11 10	9 9 10 9 12
70	10 10 10 7 10	10 10	11 10 10 9	12 10 11 17 14
65	12 12 11 10	10 11 10	11 12 9 10 12 12 9	14 14 14
60	12 12 12 12	11 11 11	10 9 11	9 14 15 15 17 13
55	14 12 12	11 12 11	15 10 15 10 11 18 16	11 11 14
50	14 14 12 13	12 13 12 14	14 11 16 13 10	15 15 13 15 14
45	15 13	14 13 13 14	13 18 15 11 14	16 14 18 16 14 14
40	25 15	15 16 15 15	17 16 14 16 12	17 14 15 15 13 18
35	26	17 17 16 18	17 18 17 13 18	17 17 15 18 18 15
30	27 25	19 18 20 20	19 21 19 20 20	17 18 17 16 17 16
25	28 20	22 25 20 23	20 23 19 23 19	17 20 18 15 17
20	43 34	30 27 28 23	28 26 25 20 22	21 20 22 21 23
15	51 37	47 40 48 34	34 33 31 26 25	26 23 23 20 20 22
10	84 65	52 44 44 40	34 33 28 27	27 24 23 23 25
5	113 110 102	69 67 54 49	42 38 34 26	32 30 28 25 24
0		198 116 76 78	61 54 48 38	43 32 39 29 26 25

(The left-hand margin of the table reads vertically: L A T I T U D E)

Table 25-4b (Continued)

LAT.	100°	125°	150°
90			
85	10	9	12 10 4 9 10 10
80	10 10 11 10 10	7 10 10 15 9	11 10 8
75	7 10 10	14 9 7	8 10 10 11 9 10 13 10
70	13 13 13 13	12 13 13 12 12	11 10 10 10
65	15 14 11 12 13	10	13 13 11 10 11
60	12 13 16 16 16	15 14 14 13	12
55	14 14 13 14 13	13 14 14 14 15	15 16
50	14 12 13 12 12	12 12 13 12 12	13 15 15 17
45	13 14 13 12 13	13 11 11 12 13	12 12 14 16 13
40	13 14 14 15 12	10 12 12 12 11	13 12 13 13 13 14
35	13 13 12 11 13	13 13 14 11 13	13 12 14 12 14 13
30	16 16 17 16 16	16 15 14 14 12	14 13 14 13 13 15
25	19 21 21 18 14	19 15 15 13 14	14 13 15 12 15 12
20	18 16 15 13 19	20 20 15 15 14	14 14 16 14 14 13
15	19 14 15 17 16	16 20 20 19 19	16 16 14 15 15 13
10	24	16 16	20 17 17 17 15 14 14 13
5		17 16	15 17 19 18 18 18 14 14
0		16	19 17 17 14 16 15

than giants. Supergiants are rare but can be seen over great distances.

25.3.1.1 Spectral Classification. The features in a normal stellar spectrum permit the classification of stars in a sequence of decreasing temperature. The main spectral characteristics of the classification scheme are listed in Table 25-5. Each spectral class is divided into 10 or more subintervals.

Table 25-5. Stellar Classification.

Class	Class Characteristics
Oxygen Stars	
O	Hot stars with He II absorption.
B	He I in absorption, H absorption stronger at later sub-classes.
A	H absorption very strong, decreasing at later sub-classes. Ca II increases with sub-class.
F	Ca II increases with sub-class, H weaker than class A, lines of metals developing.
G	Ca II strong, Fe and other metals strong, H weaker, molecular lines appear.
K	Strong metallic lines, molecular bands more pronounced.
M	Cool stars with lines of neutral metals very strong. TiO bands present and increasing with sub-class.
Carbon Stars	
R or C	Cool stars ($\simeq$ M) Strong CN and
N	C_2 bands, no TiO, metallic line spectra similar to K & M stars.
Heavy Metal Stars	
S	Cool stars ($\simeq$ M) bands of ZrO, YO and LaO, Zr and Te lines.

Ionization is denoted by Roman numerals. A neutral atom is I, singly ionized II.

A plot of absolute visual magnitude against spectral class (or temperature) for stars results in a well ordered display called the Hertzsprung-Russell diagram. Stars of different luminosity classes occupy different regions of the diagram. Thus, a two dimensional classification scheme is required, one which specifies the temperature, alternatively spectral

class, the other the luminosity, or intrinsic brightness. Table 25-6 lists the absolute visual magnitude as a function of spectral and luminosity class for normal stars.

25.3.1.2 Stellar Luminosities, Colors and Temperatures. The total power over all wavelengths emitted by a star is the luminosity, L. The effective temperature T_e of a star of radius R is related to the luminosity by

$$L = 4\pi R^2 \sigma T_e^4$$

$\sigma \equiv$ Stefan-Boltzmann constant $= 5.66956 \times 10^{-12}$ Wcm^{-2}deg^{-4}.

The apparent bolometric magnitude, m_{bol}, corresponds with the apparent luminosity of the star at the earth. The bolometric correction B.C. is the value that is added to the visual magnitude to obtain m_{bol}.

The difference in magnitudes for observations of a star in different spectral bands is called the color. The colors for dwarf and giant stars, based on the photometric system defined in Table 25-1, are listed in Tables 25-7 and 25-8, respectively, as a function of spectral type. Also included are the bolometric correction and effective temperature for each class. The absolute magnitude in any of the specified spectral bands can be calculated from the data in Tables 25-6, 25-7 and 25-8.

25.3.1.3 Infrared Stars. The dominant stellar component of the apparent background shifts to the later, and cooler, spectral types as the wavelength of observation is increased. 70% of the stars in the Two Micron Sky Survey (TMSS) of Neugebauer and Leighton [1969] are M, S, or C giants; less than 3% of the stars in the visual spectral region are this cool [Nort, 1950]. At wavelengths longward of 6 μm several new classes of objects dominate over the "normal" stellar component. These sources have low infrared color temperatures due to either an intrinsically low temperature or extinction. The discrete, isolated, starlike sources among these new objects appear to be undergoing rapid mass loss. This mass loss produces extensive dusty envelopes that contain grains of silicate, graphite, SiC, Fe or Fe_3C. The emission from the embedded star is absorbed, in part, and re-emitted in the infrared.

25.3.1.4 M Stars. M stars are recognized by the optical features outlined in Table 25-5 or by low resolution IR spectroscopy for optically faint objects. Main spectral features are the CO fundamental and first overtone at 4.7 and 2.3 μm, H_2O at 2.7 μm, and circumstellar silicates at 9.7 μm and in some cases, 18.6 μm. The silicate feature is generally in weak emission in early M stars. It becomes progressively stronger with advancing spectral subclass, and in extreme cases it is optically thick and appears as a strong absorption. Examples are given in Figure 25-6. Many of these stars exhibit OH maser emission.

Table 25-6. Absolute visual magnitude as a function of spectral and luminosity class. Compiled from data given by Keenan [1963], Walborn [1973], Conti and Alschuler [1981], Humphreys [1978], Jung [1970, 1971], Mikami [1978a,b], Joy and Apt [1974] with spectral type corrections of Wing and Yorka [1979], Keenan [1978], and Egret, Keenan and Heck [1982]. Colon denotes uncertain values.

| | Main Sequence | Subgiants | Giants | | Supergiants | | |
Type	V	IV	III	II	Ib	Iab	Ia
O3	−5.5						−7.0:
O4	−5.5		−6.4:			−6.5	−7.0:
O5	−5.5		−6.4		−6.3:	−6.4	−7.0:
O6	−5.5		−5.6		−6.3:	−6.3	−7.0:
O7	−4.8		−5.5	−5.9	−6.2	−6.3	−7.0:
O8	−4.4		−5.5	−5.9	−6.2	−6.5	−7.0:
O9	−4.3	−5.2	−5.5	−5.9	−6.2	−6.7	−7.0:
						I	
B0	−4.2	−4.6	−5.1:	−5.6:		−6.0:	
B1	−3.5	−3.9	−3.3	−5.1:		−6.0:	
B2	−2.2	−3.0	−2.2	−4.4		−6.0:	
B3	−1.3	−2.3	−1.9	−3.9		−6.0:	
B5	−1.6	−1.8	−1.6	−3.7		−6.0:	
B7	−1.5	−1.0	−1.3	−3.6		−6.0:	
B9	0.0	−0.3	−0.7	−3.1		−6.0:	
A0	0.2	0.1	−0.6	−2.8		−6.0:	
A1	0.5	0.3	−0.4	−2.6		−6.0:	
A2	0.6	0.6	−0.2	−2.4		−6.0:	
A3	0.8	0.9	0.0	−2.3		−6.0:	
A5	1.5	1.2	0.2	−2.1		−6.0:	
A7	1.6	1.5	0.6	−2.0		−6.0:	
F0	2.3	2.0	0.6	−2.0		−6.0:	
F2	2.5	2.2	1.4	−2.0		−6.0:	
F5	3.0	2.3	0.2	−2.0		−6.0:	
F6	3.2	2.3	0.0	−2.0		−6.0:	
F8	3.5	2.4	0.6			−6.0:	
G0	4.1	2.9	1.0	−2.0		−6.0:	
G2	4.3	3.0	0.6	−2.0		−6.0:	
G5	4.9	3.1	0.3	−2.0		−6.0:	
G8	4.5	3.2	0.3	−2.1		−6.0:	
K0	5.8	3.2	0.2	−2.1:		−6.0:	
K1	6.0		0.2	−2.1		−6.0:	
K2	6.2		0.1	−2.2:		−6.0:	
K3	6.5		−0.2	−2.3:		−6.0:	
K4	6.9		−0.2	−2.3:		−6.0:	
K5	7.3		−0.5	−2.3:		−6.0:	
K7	8.0		−0.6	−2.3:		−6.0:	
M0	8.3		−0.7	−2.4:		−6.0:	
M1	9.2		−0.9	−2.4:		−6.0:	
M2	10.0		−1.1	−2.4:		−6.0:	
M3	11.0		−1.1	−2.4:			
M4	12.4		−1.0	−2.4:			
M5	15.0		−0.9				
M6	16.7		−0.9:				
M7	18.0		−0.9:				
M8			−0.5:				

Absolute visual magnitude as a function of spectral and luminosity class.

Table 25-7. The Main Sequence colors compiled from data given by Johnson [1966], Aaronson, Frogel and Persson [1978], Veeder [1974], and Hayes [1978].

Spt	U-V	B-V	V-R	V-I	V-J	V-H	V-K	V-L	V-M	V-N	BC	T_{eff}
05-7	-1.46	-0.32	-0.15	-0.47	-0.73		-0.94	-1.01			-3.9	42000
08-9	-1.44	-0.31	-0.15	-0.47	-0.73		-0.94	-1.01			-3.5	34000
09.5	-1.40	-0.30	-0.14	-0.46	-0.73		-0.94	-1.00			-3.1	31900
B0	-1.38	-0.30	-0.13	-0.42	-0.70		-0.93	-0.94			-2.96	30300
B0.5	-1.29	-0.28	-0.12	-0.39	-0.66		-0.88	-0.93			-2.83	28600
B1	-1.19	-0.26	-0.11	-0.36	-0.61		-0.81	-0.86			-2.59	25700
B2	-1.10	-0.24	-0.10	-0.32	-0.55		-0.74	-0.77			-2.36	23100
B3	-0.91	-0.20	-0.08	-0.27	-0.45		-0.61	-0.63			-1.94	18900
B5	-0.72	-0.16	-0.06	-0.22	-0.35		-0.47	-0.48			1.44	15300
B6	-0.63	-0.14	-0.06	-0.79	-0.36		-0.41	-0.41			-1.17	14000
B7	-0.54	-0.12	-0.04	-0.17	-0.25		-0.35	-0.34			-0.94	13000
B8	-0.39	-0.09	-0.02	-0.12	-0.17		-0.24	-0.22			-0.61	11500
B9	-0.25	0.06	0.00	-0.06	-0.09		-0.14	-0.11			-0.31	10106
A0	0.00	0.00	0.02	-0.00	-0.01		-0.03	0.00	-0.03	-0.03	-0.15	9410
A2	0.12	0.06	0.08	0.09	0.11		0.13	0.16	0.13	0.13	-0.08	8900
A5	0.25	0.14	0.16	0.22	0.27		0.36	0.40	0.36	0.36	-0.02	8210
A7	0.30	0.19	0.19	0.28	0.35		0.46	0.52	0.46	0.46	-0.01	7920
F0	0.34	0.27	0.30	0.47	0.58		0.79	0.86	0.79	0.79	-0.01	7160
F2	0.39	0.36	0.35	0.55	0.68	0.95	0.93	1.07	0.93	0.93	-0.02	6880
F5	0.45	0.42	0.40	0.64	0.79	1.08	1.07	1.25	1.07	1.07	-0.03	6560
F8	0.55	0.50	0.47	0.76	0.96	1.29	1.25	1.45	1.27	1.27	-0.08	6190
G0	0.63	0.59	0.50	0.81	1.03	1.38	1.35	1.53	1.35	1.44	-0.10	6010
G2	0.79	0.63	0.53	0.86	1.10	1.47	1.44	1.61	1.54	1.69	-0.13	5860
G5	0.89	0.70	0.54	0.89	1.14	1.52	1.49	1.67			-0.14	5780
G8	1.06	0.74	0.58	0.96	1.24	1.60	1.63	1.85			-0.18	5580
K0	1.36	0.89	0.64	1.06	1.38	1.80	1.83	2.00			-0.24	5260
K2	1.60	0.95	0.74	1.22	1.57	2.09	2.15	2.25			-0.35	4850
K5	2.28	1.18	0.99	1.62	2.04	2.71	2.82	2.84			-0.66	4270
K7	2.52	1.37	1.16	2.00	2.43	3.13	3.25	3.40			-0.93	4030
M0	2.67	1.43	1.28	2.26	2.85	3.46	3.60	3.78			-1.21	3880
M1	2.70	1.49	1.42	2.56	3.21	3.83	4.00	4.15			-1.49	3720
M2	2.69	1.53	1.51	2.76	3.45	4.08	4.27	4.47			-1.75	3600
M3	2.70	1.58	1.61	2.83	3.72	4.36	4.57	4.85			-1.90	3480
M4	2.70	1.62	1.71	3.30	3.99	4.64	4.87	5.40			-2.28	3370
M5	2.80	1.68	1.84	3.49	4.34	5.00	5.25	5.80			-2.59	(3260)
M6	2.99	1.76	2.01	3.87	4.69	5.46	5.75	7.8			-2.93	(3140)
M7	3.24	1.87	2.26	4.42	5.34	6.16	6.50				-3.46	(2880)
M8	(3.50)	1.99	2.52	4.90	6.25	6.85	7.25	9.6			-4.00	(2620)

Most of the late M type stars exhibit nearly periodic variations of one or more magnitudes in the infrared. The period of variability correlates with the strength of the silicate emission feature [DeGiora-Eastwood et al., 1981] and with the amplitude of variability. An extreme example is AFGL 2205 with a 4 magnitude amplitude of variability at 2.2 and 3.4 μm and a 4 year period.

25.3.1.5 Carbon Stars. In addition to the features listed in Table 25-5, carbon stars are distinguished in the infrared by an absorption at 3.1 μm due to various hydrocarbons and a broad SiC dust feature near 11 μm. Figure 25-7 shows

these features for progressively cooler carbon stars. The combination strong molecular blanketing in the visual for the cooler carbon stars and circumstellar absorption make these stars optically faint. Consequently, the relative proportion of carbon stars as compared to late M stars at a given magnitude increases with increasing wavelength.

25.3.1.6 Planetary Nebulae and Related Objects. Infrared spectra of planetary nebulae show, in general, emission bands superimposed on featureless continua characteristic of heated dust. The emission bands, shown in Figure 25-8 for the planetary NGC 7027, are probably small hy-

Table 25-8. Colors for the Giant Stars, compiled from data given by Johnson [1966], Aaron, Frogel and Persson [1978], Lee [1971], Mendoza and Johnson [1965], Hayes [1978], Ridgway, Joyce, White and Wing [1980].

| Spt	U-V	B-V	V-R	V-I	V-J	V-H	V-K	V-L	V-M	V-N	BC	T_{eff}
G5	1.55	0.92	0.69	1.17	1.52		2.08	2.18	2.02	2.05		
G8	1.64	0.94	0.70	1.18	1.56		2.18	2.27	2.09	2.12		4930
K0	1.92	1.04	0.77	1.30	1.71		2.33	2.47	2.23	2.28	−0.42	4790
K1	2.13	1.10	0.81	1.37	1.80		2.48	2.61	2.36	2.39	−0.48	4610
K2	2.32	1.16	0.84	1.42	1.87		2.64	2.73	2.45	2.48	−0.53	4450
K3	2.74	1.30	0.96	1.61	2.12		2.94	3.07	2.75	2.80	−0.60	4270
K4	3.07	1.41	1.06	1.81	2.36		3.25	3.39	3.05	3.11	−0.90	4095
K5	3.34	1.54	1.20	2.10	2.71		3.67	3.83	3.47	3.54	−1.19	3980
M0	3.42	1.56	1.24	2.14	2.77		3.74	3.89	3.59	3.65	−1.28	3895
M1	3.48	1.58	1.29	2.24	2.89	3.57	3.90	4.06	3.72	3.78	−1.36	3810
M2	3.52	1.61	1.37	2.45	3.12	3.72	4.16	4.33	3.91	3.97	−1.52	3730
M3	3.46	1.62	1.52	2.82	3.53	3.96	4.63	4.81	4.39	4.45	−1.91	3640
M4	3.29	1.62	1.79	3.38	4.19	4.39	5.34	5.54	5.10	5.14	−2.55	3560
M5	3.04	1.85	2.13	4.06	4.96	5.07	6.20	6.44	6.00	6.00	−3.34	3420
M6	4.15	1.70	2.70	4.90	5.90	5.90	7.20	7.50			−4.26	3250
M7		1.80	3.95	7.00	8.30	6.87	9.85	10.38			−7.7	
M8		1.93	4.95	8.51	10.25		11.92	12.60			−8.6	
M9		2.53	5.95	10.02	12.20		14.05	14.88			−10.8	
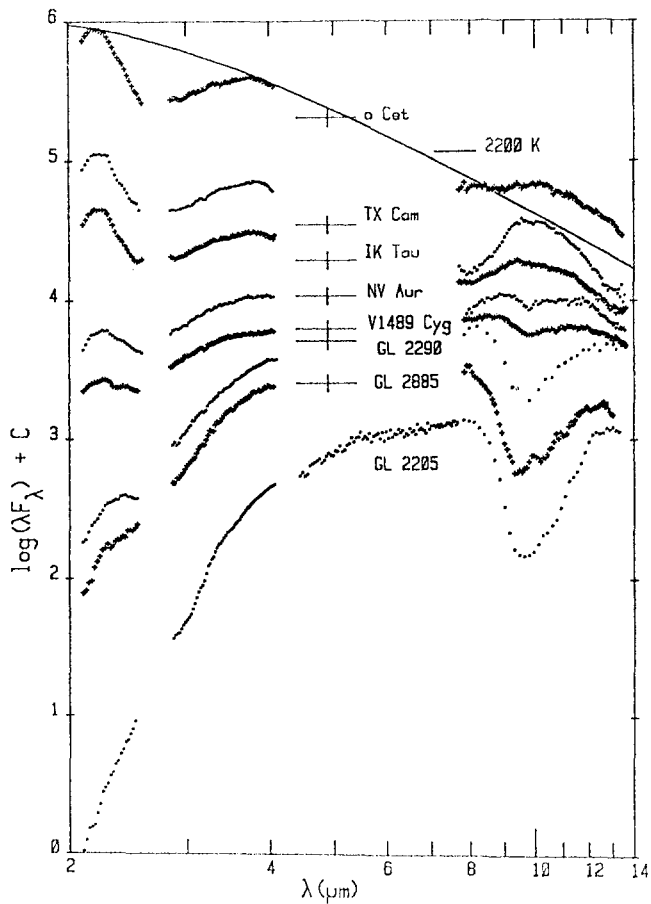
Figure 25-6. Infrared spectrophotometry of M stars illustrating the range of optical depth of the silicate feature in circumstellar envelopes [Ney and Merrill, 1980].
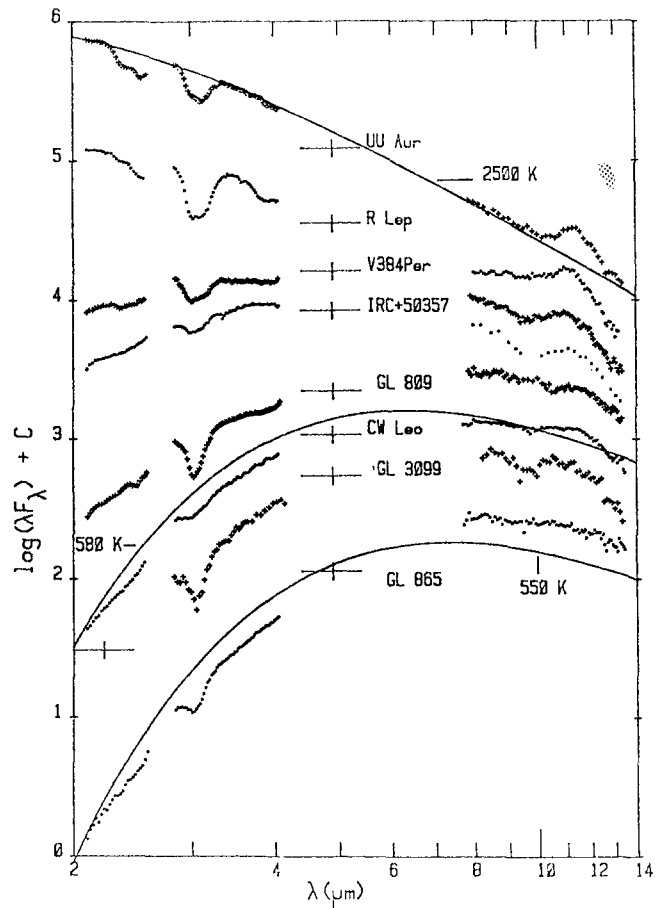

Figure 25-7. Infrared spectrophotometry of carbon stars illustrating the range of optical depths in the circumstellar envelopes associated with these objects [Ney and Merrill, 1980].
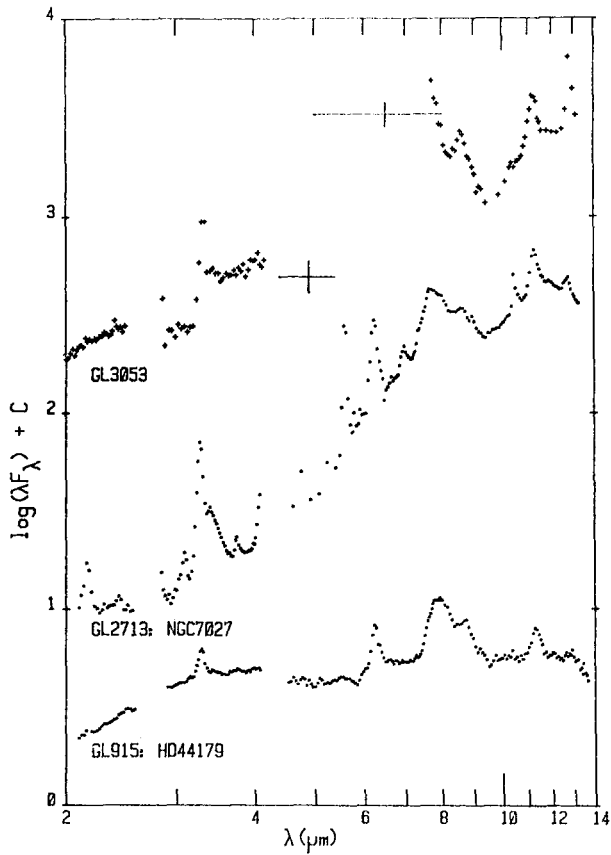
Figure 25-8. Spectrophotometry of objects with band emission from dust. NGC 7027 is identified as a planetary nebula; AFGL 915 is a disk object and AFGL 3053 is a source inside the HII region Sharpless 159 [Ney and Merrill, 1980].

drogenated carbon grains heated by UV photons [Leger and Puget, 1984]. These bands are present in the spectra of a variety of objects including compact and diffuse HII regions and the nuclei of active galaxies.

The 9.7 μm silicate band is not present in the spectra of planetary nebulae. This is consistent with the observed C/O abundance ratio in planetaries being much greater than unity. The condensates forming the dust are expected to be SiC and graphite, or possibly amorphous carbon.

Wolf-Rayet stars in the carbon sequence typically show broad continua due to heat, dust, and free-free emission of thermal electrons in their circumstellar envelopes.

Objects such as GL 915 (see Figure 25-8) exhibit disc shaped geometry, that is the circumstellar dust is confined to a plane. They are bright infrared sources but the visual properties of the exciting star depend on the geometry of the observation. GL 618 and 2688 are infrared sources with the central star obscured by the disk of dust. Optical observation of GL 2688 nebulosity above and below the dust lane show a highly reddened spectrum of an F5-Ia star. GL 915 is seen more nearly pole on and the spectra of the B9II-III star can be measured directly.

25.3.1.7 Luminous Stars with Infrared Excesses.
Low excitation emission-line objects, hot supergiants and other types of stars earlier than M are included in this category. Be stars with T $\geq$ 13 000 K often show an excess of infrared due to free-free emission in a hot (T $\geq$ 10 000 K) circumstellar plasma shell [Gehrz et al., 1974]. The infrared excess, in general, decreases at the later spectral types. An optically thin dust shell enhances the infrared emission around some hot supergiants. The shell condenses from the mass lost by the star.

25.3.2 Gas and Dust

The galactic gas and dust is confined to the galactic plane with a thickness of about 200 parsecs. The distribution is patchy, with concentrations of matter in interstellar and molecular clouds. The interstellar gas is composed primarily of hydrogen, which is detected by the 21 cm emission in the hyperfine structure of neutral atomic hydrogen. The gas clouds tend to be along the spiral arms of the galaxy and mapping at 21 cm is used to define this structure. A number of other elements in the interstellar gas are observed by their atomic lines in the visual and ultraviolet and molecular lines in the radio region.

Dust is mixed with the interstellar gas. The dust may be composed of bare graphite grains plus grains of silicates and/or iron with water ice mantles. In some of the denser clouds, water ice absorption at 3.07 μm and the silicate feature at 9.7 μm has been observed. The interstellar absorption of starlight is almost entirely due to dust.

25.3.2.1 Interstellar Extinction.
In Section 25.1.3 it was seen that the interstellar absorption, in magnitudes, was required to relate the observed apparent magnitude of a star to its absolute magnitude. From Table 25-9, the amount of absorption depends on the wavelength, in general decreasing with wavelength. This wavelength dependence is called in-

Table 25-9. Average interstellar absorption, in magnitudes, normalized to the visual with A_v = 1.0. Data from Johnson [1968] and Becklin et al. [1978].

λ(μm)	A_λ/A_v	λ(μm)	A_λ/A_v
0.365 (U)	1.58	1.65 (H)	0.16
0.4	1.45	2.22 (K)	0.09
0.44 (B)	1.32	3.5 (L)	0.05
0.5	1.13	4.8 (M)	0.03
0.553 (V)	1.00	8.7	0.06
0.67	0.67	9.5	0.13
0.9 (I)	0.46	11.2	0.09
1.0	0.38	12.5	0.04
1.25 (J)	0.26	20.0 (Q)	0.03

Colors from Table 25-1 that correspond to the listed wavelengths are indicated in parentheses.

terstellar reddening; a star will appear redder than it is due to the interstellar absorption.

Near the sun the average out of the plane extinction is [Milne and Aller, 1980]

$$C = k_o \, w(1 - e^{-r\sin|b|/w}) \cosec |b| \quad (25.12)$$

b = galactic latitude,

k_o = 1.75 visual magnitudes per kiloparsec,

r = radial distance from the sun, and

w = scale height of absorbing material

    = 0.119 kpc   b > 0°

       0.086 kpc   b < 0°.

Large scale extinction in the galaxy can be estimated from the observed gas distribution and the fact that interstellar reddening is correlated with the total column density of hydrogen [Savage and Mathis, 1979].

25.3.2.2 HII Regions. An HII region is an optically bright gaseous nebula excited by an O or early B type star or a cluster of such stars ($T_c > 15\,000$ K). The stellar ultraviolet radiation photoionizes the surrounding gas; hydrogen is almost completely ionized, helium predominately singly ionized, and other elements singly or doubly ionized. The ionized electrons are collisionally thermalized to a kinetic temperature of about 10 000 K. Recombination of the thermal electrons and ions produces emission line spectra including forbidden lines.

Compact HII regions are the smallest gaseous nebulae and are considered to be young objects. Diffuse HII regions are an order to magnitude larger in size than the compact HII regions and considerably more rarified. Extended HII regions are very large and have low density; they overlap to a considerable degree forming a hot, tenuous plasma in the galactic plane. All of these objects emit copious infrared radiation. A major fraction of the ultraviolet luminosity of these sources is absorbed by the dust in and around the HII region and then is converted into the infrared. Generally, the infrared intensity peaks at about 70 μm but spectral distribution is broader than dust emitting at a single temperature. The dust and gas are well mixed as the radio flux from free-free emission from the ionized HII region correlates with the reradiated 11 μm flux. HII regions are among the strongest infrared sources in the galaxy at wavelengths longer than 10 μm.

25.3.3.3 Molecular Clouds. Molecular clouds are dense, cool clouds of interstellar gas and dust in which a number of molecular lines have been detected. The clouds may be divided into those which have a peak gas temperature measured by CO emission of $T_k < 20$ K throughout the region

and those which are warmer. The second group ($T_k > 20$ K) require additional heat sources to explain the observed temperature, the first does not. The second group also has evidence of recent star formation such as compact HII regions and infrared sources.

Typical spectra for infrared sources in molecular clouds show red continua with strong ice and silicate absorption as seen in Figure 25-9. The emission of the cloud as a whole is characteristic of a much cooler temperature, peaking near 100 μm.
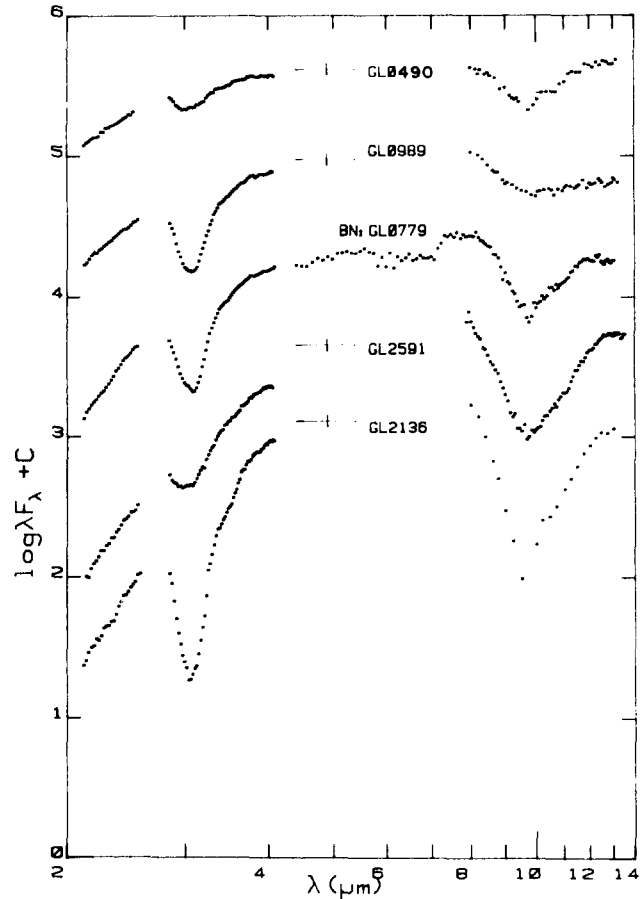

Figure 25-9. Spectrophotometry of source in molecular clouds. The prominent features are "ice" at 3.15 μm and the 10 μm silicate absorption [Ney and Merrill, 1980].

25.4 EXTRAGALACTIC OBJECTS

Galaxies are usually classified according to morphology. Ellipticals are elliptical in shape and arranged in a sequence of apparent ellipticity, from circular to most elongated. Spiral galaxies are in a sequence according to the relative sizes of the nuclear bulge and disk and details of the spiral structure in the disk. Early spiral galaxies have a large nuclear bulge and a small disk with tightly wound spiral arms. As

the classification scheme advances, the bulge decreases, the disk increases, and the arms open. At the end of this sequence are the irregular galaxies with little or no central condensation and little or no order to the disk.

Apart from this standard classification there are galaxies that are more condensed than normal systems. These objects can be classified along a continuum as to degree of compactness, the open Seyfert galaxies at one end and quasi-stellar objects (QSOs) at the other. The Seyferts are almost normal galaxies with an intensely bright and compact core. By definition QSO appear stellar on photographs on a plate scale used for surveys.

Infrared emission is a general feature in the nuclei of Seyfert galaxies. The infrared flux accounts for most of the total luminosity for many of these galaxies, and a significant portion of the QSO and BL Lac objects are intrinsically bright in the infrared. The emission from these objects can in general be represented by a power law through the visual and well into the infrared. This indicates a non-thermal cause, possibly noncoherent synchrotron emission, for these sources.

An unbiased infrared survey [de Jong et al., 1984] found that most of the infrared emission from galaxies is longward of 50 μm. The infrared emission is strongly correlated with the type of galaxy. Elliptical galaxies and lenticulars (SO) have little or no infrared emission in excess of the normal stellar component. The infrared excess increases with advancing galactic type, with late type spirals emitting as much as five times more infrared than visual energy. An infrared to visual energy ratio as large as 50 has been found for some optically faint unidentified galaxies [Soifer et al., 1984]. The more infrared luminous galaxies tend to be warmer ($T_{IR} \sim 50$ K) than weak infrared galaxies ($T_{IR} \sim 25$ K).

25.5 THE INFRARED CELESTIAL BACKGROUND

The infrared celestial background can be divided into three physical structures—the diffuse zodical emission, the sources in our galaxy, and external galaxies. The relative importance of these constituents depends on the wavelength. Currently, the observational data base is reasonably complete to a magnitude $M(\lambda) < 4$–4.5 over the spectral region from 2–30 μm.

25.5.1 2–8 μm

Late type giant stars dominate the background at these wavelengths. The zodiacal background is at a minimum being in the spectral crossover region between reflected sunlight and thermal emission. There are about 7300 stars brighter than m (2.2 μm) $\leq$ 3 in the sky and roughly

26 000 objects brighter than m (2.2 μm) $\leq$ 4 [Hughes, 1970]. At m (2.2 μm) = 4 a typical M giant can be seen to a distance of about 1 kpc and a late K giant star out to 0.4 kpc. These distances exceed the 0.3 kpc scale height of the galactic disk. Thus, the concentration of stars to the galactic plane increases as the limiting magnitude is increased as most of the brighter giants have been detected toward the galactic poles by m (2.2 μm) $\leq$ 4. The contrast in areal densities in the galactic plane within 30° of the center and the pole is about 6 for m (2.2 μm) < 3 and 100 for m (2.2 μm) < 6.8.

For a field of view larger than 1 μsr the large stellar density near the galactic plane produces a diffuse background due to the aggregate of all the stars along the line of sight. This background is almost constant out to 30° from the center at 6×10^{-10}Wcm$^{-2}\mu$m^{-1}sr^{-1} at 2.4 μm and 1.5×10^{-10} Wcm^{-2} μm^{-1}sr^{-1} at 4.2 μm. The brightness falls off almost exponentially at greater latitudes. The latitudinal cross section of this emission is almost gaussian with a full width at half maximum of 3°.5 at 2.4 μm and 2°.5 at 4.2 μm.

The stellar source counts to reasonably faint levels (M $\leq$ 9) in the 2–5 μm spectral region can be modeled by a disk distribution of stars [Elias, 1978; Jones et al., 1981] with components divided by spectral and luminousity classes. This model has the density of the ith component at R kpc from the sun in the (l, b) direction varying exponentially with an in plane distance, x, from the galactic center with a scale height of 2.5 kpc and perpendicular to the plane, $|z|$, with a scale height Z_i. Normalized to the solar neighborhood, the density is

$$\rho_i = \exp [(8.5 - x)/2.5 - |z|/Z_i]$$

$$r = (x^2 + z^2)^{1/2}$$

$$= \text{the galacto-centric distance of a point } (R, l, b,) \text{ from the sun}$$

$$= R \sin b$$

$$x^2 = 8.5^2 + R^2 \cos^2 b - 17 R \cos b \cos l$$

the sun is 8.5 kpc from the galactic center.

The luminosity function (No. of stars kpc^{-3}mag^{-1}) of the giant and supergiant stars is assumed to be gaussian

$$\phi_i (M) = \frac{N_i}{(2\pi)^{1/2}\sigma} \exp [-(M - \overline{M}_i)/2\sigma_i^2]$$

N_i = source density of the ith component in the solar neighborhood

$\overline{M}_i$ = mean absolute magnitude component

σ_i = dispersion in absolute magnitude component.

Values for these parameters [Elias, 1978; Jones et al., 1981] are

Spectral Class	$\overline{M}_i$ (mag)	σ_i (mag)	log (N_i) (No. stars kpc^{-3})	Z_i (kpc)
F8-G2 III	0.45	1.0	4.65	0.50
G5 III	−0.08	1.0	4.65	0.50
G8 III	−0.56	0.8	5.20	0.25
K0,1 III	−0.80	0.7	5.23	0.30
K2,3 III	−1.66	0.7	5.23	0.30
K4,5 III	−3.36	0.6	4.28	0.30
M0 III	−4.16	0.6	3.48	0.30
M1 III	−4.40	0.6	3.13	0.30
M2 III	−4.76	0.6	3.13	0.30
M3 III	−5.23	0.6	3.13	0.30
M4 III	−6.04	0.6	3.00	0.30
M5 III	−6.90	0.5	3.00	0.30
M6 III	−7.90	0.5	2.45	0.30
M7 III	−8.90	0.5	2.09	0.30
M8+III	−9.90	0.5	1.65	0.30
A-G I-II	−7.00	2.0	1.53	0.5
K-M2 I-II	−9.50	1.0	1.49	0.5
M3-M4 I-II	−11.00	1.0	1.10	0.5

Dwarf stars [after Mamon and Soneira, 1982]

$$\phi_d \begin{cases} = 0 & M < -10 \\ = 10^7 * 10^{0.01M} [1 + 10^{-0.19(M-2)}]^4 & -10 \leqslant M \leqslant 9 \\ = 3 \times 10^{-7} \exp[-(M/9)^2] & M \geqslant 9 \end{cases}$$

with $Z_i = 0.09$ kpc $M \leqslant 1.5$

0.325 kpc $M \geqslant 3.5$

and linear interpolation between.

The number of stars brighter than apparent magnitude m in solid angle dω in the (1,b) direction is

$$N(m,1,b)d\omega = d\omega \int_{-\infty}^{m} dm' \int_{o}^{\infty} R^2 [\Sigma \; \rho_i(r,M)\phi_i(M)]dR$$

$$M = m - 5 \log_{10}(R) - A(R) - 10. \qquad (25.13)$$

The interstellar extinction A(R) is given by (see also Equation (25.11))

$$\delta \; A(R)/\delta R = 0.07 \; (2.2/\lambda)^2 \exp[(8.5 - x)/3.7 - |z|/0.1].$$

The in plane scale height of the dust is 3.7 kpc and the exponential thickness is 0.2 kpc.

Table 25-10. Number of sources per square degree brighter than a given magnitude (from the model in Section 25.5).

Mag/(1,b)	(0,0)	(20,0)	(60,0)	(180,00)	(30,0)	pole
			2.2 μm			
1	0.2	0.2	0.2	0.1	0.01	0.008
2	1.2	1.1	0.7	0.2	0.1	0.03
3	4.4	4.4	2.3	0.6	0.2	0.07
4	14.2	14.5	6.7	1.6	0.5	0.2
5	42.4	42.7	17.9	4.0	1.2	0.5
6	122.7	116.3	45.9	9.9	2.9	1.1
7	359.3	297.7	113.4	24.6	7.1	2.4
8	975.1	730.0	274.7	61.8	16.0	4.8
9	2489.5	1750.1	670.0	156.9	33.3	9.6
10	6339.0	4238.4	1688.0	396.5	65.7	20.7
			11 μm			
1	33.8	29.1	4.6	0.4	0.02	0.009
2	120.5	101.9	13.4	0.9	0.08	0.03
3	286.0	242.0	27.7	1.7	0.2	0.07
4	496.0	420.9	45.0	3.1	0.5	0.2
5	768.0	625.2	68.6	5.9	1.2	0.5
6	1278.7	967.9	112.7	12.4	3.1	1.2
7	2445.4	1723.4	212.6	28.7	7.6	2.8
8	5499.9	3563.1	447.4	70.4	17.7	6.4
9	11423.7	7408.2	1006.2	179.8	40.0	15.9
10	24420.6	15996.2	2477.3	465.6	91.1	45.8

The emission observed at 2.4 μm from the stellar component for the nuclear bulge has been modeled [Martiara et al., 1978] as

$$I(r) = 6.2 \times 10^{34} \text{ w } \mu m^{-1} \text{ kpc} \frac{\exp(-r/2.5)}{(r^2 + 0.14^2)}$$

with

$$r = x^2 + (z/0.52)^{2 \; 1/2}. \qquad (25.14)$$

Source counts predicted by this model are given in Table 25-10.

25.5.2 8–30 μm

The thermal emission from the zodiacal dust, the asteroids, and most planets peak in this spectral region. The asteroids and planets without atmospheres have grey body spectral energy distributions with equilibrium temperatures characterized by their distance from the sun (Section 25.2). The zodiacal emission (Section 25.2.4) is the brightest component of the diffuse background.

The brightest classes of galactic objects at these wavelengths are stars embedded in circumstellar dust shells and compact HII regions. These objects absorb the visual and ultraviolet emission of the embedded stars and reradiated the energy in the infrared. These objects are intrinsically very luminous and are detectable over large distances. As a class the circumstellar dust shell source has a mean absolute 11 μm magnitude of − 12, a one magnitude dispersion about the mean, a density of 90 sources per kpc^3 in the polar neighborhood and a perpendicular scale height of 300 pc [Grasdalen et al., 1983]. A 400 K color temperate for the emission provide reasonable extrapolation to other wavelengths.

The HII regions can be characterized by a mean absolute 11 μm magnitude of − 18, a 2.0 magnitude dispersion, a density of 10 sources per kpc^3 in the solar neighborhood.

There are about 350 000 stars brighter than 4.5 magnitudes in the 8–30 μm region. The source density at this magnitude limit out of the galactic plane is about 1 star per square degree. About half of these objects are identified with stars in various catalogs most of which have K and M spectral classifications [Rowan-Robinson et al., 1984].

The predicted source counts based on the model in the previous section and including HII regions and star with circumstellar dust shells are given in Table 25-10.

CHAPTER 25

REFERENCES

Aaronson, M., J.A. Frogel, and S.E. Persson, Photometric Studies of Composite Stellar Systems. II. Observations of H₂O Absorption and the Coolest Stellar Component of E and SO Galaxies," *Astrophys. J.*, **220**: 442, 1978.

Allen, C.W., *Astrophysical Quantities*, Athlone Press, 1973.

Allen, D.A., "Infrared Studies of the Lunar Terrain," PhD Thesis, University of Cambridge, 1970.

Allen, D.A. and T.L. Murdock, "Infrared Photometry of Saturn, Tatan and the Rings," *Icarus*, **14**: 1–2, 1971.

Allen, D.A. and E.P. Ney, "Lunar Thermal Anomalies: Infrared Observations," *Science*, **164**: 419, 1969.

Becklin, E.E., K. Mathews, G. Neugebauer, and S.P. Willner, "Infrared Observations of the Galactic Center. I. Nature of the Compact Sources," *Astrophys. J.*, **219**: 121, 1978.

Conti, P.S. and W.R. Alschuler, "Spectroscopic Studies of O-Type Stars. I. Classification and Absolute Magnitudes," *Astrophys. J.*, **170**: 325, 1971.

Courtin, R., D. Gautier, and A. Lacombe, "On the Thermal Structure of Uranus from Infrared Measurements," *Astron. Astrophys.* **63**: 97–101, 1978.

DeGiora-Eastwood, K., J.A. Hackwell, G.L. Grasdalen, R.D. Gehrz, "A Correlation Between Infrared Excess and Period for Mira Variables," *Astrophys. J. (Ltrs)*, **245**: L75, 1981.

Egret, D., P.C. Keenan, and A. Heck, "The Absolute Magnitudes of G5–M3 Stars near the Giant Branch," *Astron. Astrophys.*, **106**: 115, 1982.

Elias, J. H., "A Study of the IC 5146 Dark Cloud Complex," *Astrophys. J.*, **223**: 859, 1978.

Erickson, E. F., D. Goorvitch, J. P. Simpson, and D. W. Strecker, "Far Infrared Spectrophotometry of Jupiter and Saturn," *Icarus*, **35**: 61–73, 1978.

Gehrz, R.D., J.A. Hackwell, and G.L. Grasdalen, "Infrared Studies of AFGL Sources," AFGL TR-79-0274, ADA 084713, 1979.

Gehrz, R.D., J.A. Hackwell, and G.L. Grasdalen, "Infrared Observations of Be Stars from 2.3 to 19.5 Microns," *Astrophys. J.*, **191**: 675, 1974.

Gillett, F.C. and W.J. Forrest, "The 7.5–13.5 μm Spectrum of Saturn," *Astrophys. J.*, **187**: L37–L38, 1974.

Gillett, F.C. and K.M. Merrill, "The 7.5–13.5 μm Spectra of Ceres and Vesta," *Icarus*, **26**: 358–360, 1975.

Gillett, F.C. and G.H. Rieke, "5-20 Micron Observations of Uranus and Neptune," *Astrophys. J.*, **218**: L141–144, 1977.

Gradie, J. and E. Tedesco, "Compositional Structure of the Asteroid Belt," *Science*, **216**: 1405–1407, 1982.

Grasdalen, G.L., R.D. Gehrz, J.A. Hackwell, M. Castelaz and C. Gullinson, "The Stellar Component of the Galaxy as seen by the AFGL Infrared Sky Survey," *Astrophys. J. Suppl.*, **53**: 413, 1983.

Hanel, R., B. Conrath, F.M. Flaser, V. Kunde, W. Maguire, J. Pearl, J. Pirraglia, R. Samuelson, L. Herath, M. Allison, D. Cruikshank, D. Gautier, P. Gierasch, L. Horn, R. Koppany, and C. Ponnamperuma, "Infrared Observations of the Saturnian System from Voyager 1," *Science*, **212**: 192–200, 1982.

Hansen, O., "An Explication of the Radiometric Method for Size and Albedo Determination," *Icarus*, **31**: 456–482, 1977.

Hauser, M.G., F.C. Gillett, F.J. Low, T.N. Gautier, C.A. Beichmann, G. Neugebauer, H.A. Aumann, B. Baud, N. Boggess, J.P. Emerson, J.R. Houck, B.T. Soifer, and R.G. Walker, "IRAS Observations of the Diffuse Infrared Background," *Astrophys. J. (Ltrs)*, **279**: L15, 1984.

Hayes, D.S., "The Absolute Calibration of the HR Diagram: Fundamental Effective Temperatures and Bolometric Corrections," IAU Symposium 80 *The HR Diagram*, edited by A.G. Davis Philip and D.S. Hayes, 65, 1968.

Hayes, D.S. and D.W. Latham, "A Rediscussion of the Atmospheric Extinction and the Absolute Spectral Energy Distribution of Vega," *Astrophys. J.*, **197**: 593, 1975.

Humphreys, R.M., "Studies of Luminous Stars in Nearby Galaxies. I. Super-giants and O Stars in the Milky Way," *Astrophys. J. Suppl*, **38**: 309, 1978.

Ingersoll A.P., G.S. Orton, G. Münch, G. Neugebauer, and S.C. Chase "Pioneer II Infrared Radiometer Experiment: The Global Heat Balance of Jupiter," *Science*, **188**: 472, 1975.

Ingersoll et al., "Pioneer Saturn Infrared Radiometer: Preliminary Results," *Science*, **207**: 439, 1980.

Johnson, H.L., "Interstellar Extinction in the Galaxy," *Astrophys. J.*, **141**: 923, 1965.

Johnson, H.L., "Astronomical Measurements in the Infrared," *Ann. Rev. Astron. Astrophys.*, **4**: 193, 1966.

Johnson, H.L., "Nebulae and Interstellar Matter: Interstellar Extinction," edited by B.M. Middlehurst and L.H. Allen, Ch. 5, 167, 1978.

Jones, T.J., M. Ashley, A.R. Hyland and A. Ruelas-Mayorga, "A Search for the Infrared Counterpart of Type II OH Masers-I. A Model for the IR Background Source Confusion," *Mon. Not. R. Astr. Soc.*, **197**: 413, 1981.

Joy, A.H. and H.A. Abt, "Spectral Types of M Dwarf Stars," *Astrophys. J., Suppl.*, **28**: 1, 1974.

Jung, J., "The Derivation of Absolute Magnitudes from Proper Motions and Radial Velocities and the Calibration of the HR Diagram II," *Astron. Astrophys.*, **4**: 53, 1970.

Keenan, P.C., "Classification of Stellar Spectra," *Basic Astronomical Data*, Ch. 8, edited by K. A. Strand, University of Chicago Press, 78, 1963.

Keenan, P.C., "A More Accurate HR Diagram for the Cooler Stars," IAU Symposium 80, "The HR Diagram," edited by A.G. Davis Philip and D.S. Hayes, 13, 1978.

Lee, T.A., "Photometry of High-Luminosity M-Type Stars," *Astrophys. J.*, **162**: 217, 1970.

Leger, A. and J.L. Puget, "Identification of the Unidentified IR Emission Features of Interstellar Dust?" Astron. Astrophys., **137**: L5, 1984.

Leinert, C., "Zodiacal Light—A Measurement of the Interplanetary Medium," *Space Sci. Rev.*, **18**: 281–339, 1975.

Levan, P.D. and S.D. Price, "85 μm Fluxes from Asteroids: 2 Palles, 7 Iris, 15 Eunamia, and 45 Eugenia," *Icarus*, **57:** 35, 1984.

Low, F.J., "Ground Based Infrared Measurements," AFCRLTR-73-0371, AD768620 1973.

Low, F.J., D.A. Beintoma, T.N. Gautier, F.C. Gillett, C.A. Beckman, G. Neugebauer, E. Young, H.H. Aumann, N. Boggess, J.D. Emerson, H.J. Habing, M.G. Hauser, J.R. Houck, M. Rowan-Robinson, B.T. Soifer, R.G. Walker and Wesselius, "Infrared Cirrus: New Components of the Extended Infrared Emission," *Astrophy. J. (Ltrs)*, **278:** L19, 1984.

Maihara, T., N. Oda, T. Sugujama, and H. Okuda, "2.4 — Micron Observation of the Galaxy and Galactic Structure," *Publ. Astron. Soc. Japan*, **30:** 1, 1978.

Mamon, G.A. and R.M. Soneira, "Stellar Luminosity Functions in the R, I, J and K Bands Obtained by Transformation from the Visual Band," *Astrophys. J.*, **225:** 181, 1982.

Mendoza V., E.E. and H.L. Johnson, "Multicolor Photometry of Carbon Stars," *Astrophys. J.*, **141:** 161, 1965.

Mikami, T., "Absolute Magnitudes of M-Type Stars in the Solar Neighborhood," *Publ. Astron. Soc. Japan*, **30:** 191, 1978a.

Mikami, T., "Absolute Magnitudes of F-, G- and K-Type Stars in the Solar Neighborhood," *Publ. Astron. Soc. Japan*, **30:** 207, 1978b.

Milne, D.H. and L.H. Aller, "An Average Model for Galactic Absorption," *Astron. J.*, **85:** 17, 1980.

Murdock, T.L., "Mercury's Infrared Phase Effect," *Astron. J.*, **79:** 1457–1464, 1964.

Murdock, T.L. and E.P. Ney, "Mercury: The Dark Side Temperature," *Science*, **170:** 535–537, 1970.

Murdock, T.L. and S.D. Price, "Measurements of Infrared Zodiacal Light: *Astron. J.*, in press, 1985.

Neugebauer, G. and R.B. Leighton, "Two Micron Sky Survey: A Preliminary Catalog," NASA SP-3047, 1969.

Ney, E.P., "Multiband Photometry of Comets Kahoutek, Bennett, Bradfield and Encke," *Icarus* **23:** 551–560, 1974.

Ney, E.P. and K.M. Merrill, "Study of Sources in AFGL Rocket Infrared Study," AFGL TR-80-0050, ADA 084098, 1980.

Nolt, I.G., A. Tokunaga, F.C. Gillett, and J. Caldwell, "The 22.7 Micron Brightness of Saturns Rings Versus Declination of the Sun," *Ap. J.*, **219:** L63, 1978.

Nort, H., "The Stars of Six Spectral Classes and the Milky Way," *Bull. Astron. Neth.*, **11:** 181, 1950.

Pikkarainen, T., "The Surface Structures of the Moon and Mercury Derived from Integrated Photometry," *Ann. Acad. Sci. Fenn.*, **A6:** 316, 1969.

Price, S.D., L.P. Marcotte, and T.L. Murdock, "Infrared Observation of the Zodiacal Dust Cloud," *Astron. J.*, **85:** 765–771, 1980.

Reed, R.A., W.J. Forrest, J.R. Houck, and J.B. Pollack, "Venus: The 17-38 Micron Spectrum," *Icarus*, **33:** 554–557, 1978.

Ridgeway, S.T., R.R. Joyce, N.M. White, and R.F. Wing, "Effective Temperatures of Lefe-Type Stars: The Field Giants from K0 to M6," *Astrophys. J.*, **235:** 126, 1980.

Rowan-Robinson, M., P. Clegg, C. Beichmann, G. Neugebauer, B.T. Soifer, H.H. Aumann, D. Beintema, N. Boggess, J. Emerson, N. Gautier, F. Gillett, M. Hauser, F. Low, and R. Walker, "The IRAS Minisurvey" *Astrophys. J. (Ltrs)*, **278:** L7, 1984.

Ryadov, U.Y., N.I. Furashov, and G.A. Sharonov, "Measurements of the Moon's Natural Infrared Thermal Emission," *Astron. Zh.*, **41:** 112, 1964.

Savage, B.D. and J.S. Mathis, "Observed Properties of Interstellar Dust," *Ann Rev. Astron. Astrophys.*, **73:** 1979.

Shorthill, R.W. and J.M. Saari, "Non-uniform Cooling of the Eclipsed Moon," *Science*, **150:** 210–212, 1965.

Smith, B.A., L. Soderblom, R. Beebe, J. Boyce, G. Briggs, A. Bunker, S.A. Collins, C.J. Hansen, T.V. Johnson, J.L. Mitchell, R.J. Terrile, M. Carr, A.F. Cook II, J. Cuzzi, J.B. Pollack, G.E. Danielson, A. Ingersoll, M.E. Davies, G.E. Hunt, H. Masurshy, E. Shoemaker, D. Morrison, T. Owen, C. Sagan, J. Veverka, R. Stone, V.E. Suomi, "Encounter with Saturn: Voyager 1 Imaging Science Results," *Science*, **212:** 163–191, 1981.

Soifer, B.T., J.R. Houck and M. Harwit, "Rocket Infrared Observations of the Interplanetary Medium," *Ap. J. Ltrs.*, **168:** L73, 1971.

Stier, M.T., W.A. Traub, G.G. Fazio, E.L. Wright, and F.J. Low, "Far Infrared Observations of Uranus, Neptune and Cere," *Astrophys. J.*, **226:** 347–349, 1978.

Tokunaga, A., Knacke, R.F., and Owen, T., "17-25 μm Spectra of Jupiter and Saturn," *Astrophys. J.*, **213:** 569–574, 1977.

Tug, H., N.M. White, and G.W. Lockwood, "Absolute Energy Distributions of α Lyrae and 109 Virginis from 3295 Å to 9040 Å," *Astron. Astrophys*, **61:** 679, 1977.

Upgren, A.P., "New Parallaxes for Old: A Coming Improvement in the Distance Scale of the Universe," *Pub. Astron. Soc. Pac.*, **9:** 143, 1980.

Veeder, G.J., "Luminosities and Temperatures of M Dwarf Stars from Infrared Photometry," *Astron. J.*, **79:** 1056, 1974.

Walborn, N.R., "Space Distribution of the O Stars in the Solar Neighborhood," *Astron. J.*, **78:** 1067, 1973.

Ward, D.B., G.E. Gull, and M. Harwit, "Far Infrared Spectral Observations of Venus, Mars and Jupiter," *Icarus*, **30:** 295–300, 1977.

Wing, R.F. and S.B. Yorka, "Comparisons of Temperature Classes Obtained by Spectroscopic and Photometric Technique: M Dwarfs, Giants and Supergiants," IAU Colloquium 47, *Spectral Classification of the Future*, edited by McCarthy, Philip, Coyne, Vatican Obs., 1979.

Wright, E.N., "Recalibration of the Far Infrared Brightness Temperatures of the Planets," *Astrophys. J.*, **210:** 250–262, 1976.